J. Fluid Mech. (2007), *vol.* 575, *pp.* 267–305.
doi:10.1017/S0022112006004411 Printed in the United Kingdom

Vorticity structure and evolution in a transverse jet

YOUSSEF M. MARZOUK† AND AHMED F. GHONIEM

Department of Mechanical Engineering, Massachusetts Institute of Technology, Cambridge, MA 02139, USA

(Received 29 April 2005 and in revised form 18 September 2006)

Transverse jets arise in many applications, including propulsion, effluent dispersion, oil field flows, and V/STOL aerodynamics. This study seeks a fundamental, mechanistic understanding of the structure and evolution of vorticity in the transverse jet. We develop a high-resolution three-dimensional vortex simulation of the transverse jet at large Reynolds number and consider jet-to-crossflow velocity ratios r ranging from 5 to 10. A new formulation of vorticity-flux boundary conditions accounts for the interaction of channel wall vorticity with the jet flow immediately around the orifice. We demonstrate that the nascent jet shear layer contains not only azimuthal vorticity generated in the jet pipe, but wall-normal and azimuthal perturbations resulting from the jet–crossflow interaction. This formulation also yields analytical expressions for vortex lines in the near field as a function of r.

Transformation of the cylindrical shear layer emanating from the orifice begins with axial elongation of its lee side to form sections of counter-rotating vorticity aligned with the jet trajectory. Periodic roll-up of the shear layer accompanies this deformation, creating complementary vortex arcs on the lee and windward sides of the jet. Counter-rotating vorticity then drives lee-side roll-ups in the windward direction, along the normal to the jet trajectory. Azimuthal vortex arcs of alternating sign thus approach each other on the windward boundary of the jet. Accordingly, initially planar material rings on the shear layer fold completely and assume an interlocking structure that persists for several diameters above the jet exit. Though the near field of the jet is dominated by deformation and periodic roll-up of the shear layer, the resulting counter-rotating vorticity is a pronounced feature of the mean field; in turn, the mean counter-rotation exerts a substantial influence on the deformation of the shear layer. Following the pronounced bending of the trajectory into the crossflow, we observe a sudden breakdown of near-field vortical structures into a dense distribution of smaller scales. Spatial filtering of this region reveals the persistence of counter-rotating streamwise vorticity initiated in the near field.

1. Introduction

The transverse jet – a jet issuing normally into a uniform crossflow – appears in a variety of applications, ranging from industrial and airborne gas turbines to oil field flows, effluent dispersion, and V/STOL aerodynamics. The flow structures, dynamics, and mixing properties of the transverse jet have therefore been the subject of numerous investigations, both experimental and computational.

† Present address: Sandia National Laboratories, Livermore, CA 94551, USA.

Early studies offered broad characterizations of the flow, measuring jet trajectories over a range of flow parameters, and developing correlations or scaling laws (Keffer & Baines 1962; Pratte & Baines 1967; Kamotani & Greber 1972). Others focused on key vortical features of the flow field, modelling the far field as a counter-rotating vortex pair and predicting its evolution with analytical arguments, for instance (Broadwell & Breidenthal 1984; Karagozian 1986). More recent studies have used velocimetry and flow visualization to develop detailed portraits of the mean and instantaneous flow structure (Kelso, Lim & Perry 1996; Smith & Mungal 1998; Hasselbrink & Mungal 2001*b*). With this information has come an increased understanding of vorticity generation in the flow. Fric & Roshko (1994) demonstrate that vorticity originating in the wall boundary layer is the source of upright vortices in the wake of the jet. Kelso *et al.* (1996) and later Lim, New & Luo (2001) describe the roll-up and folding of vortex rings on the jet shear layer, but offer different interpretations of these flow structures and of their role in initiating a counter-rotating vortex pair. We argue below that the mechanisms postulated in these and other studies of the jet shear layer (Yuan, Street & Ferziger 1999; Sykes, Lewellyn & Parker 1986) are incomplete, in part because they are restricted to Eulerian diagnostics of essentially Lagrangian phenomena. Cortelezzi & Karagozian (2001) surmount some of these difficulties by using a Lagrangian vortex method to simulate the evolution of vorticity on the shear layer and the formation of the counter-rotating vortex pair. Nonetheless, this study is subject to certain limitations. Results are somewhat limited in numerical resolution and primarily describe the transient, early-stage dynamics of the jet. More importantly, the shear layer immediately above the jet orifice is assumed to contain only azimuthal vorticity generated in the jet pipe. We will demonstrate that this assumption leads to near-field trajectories that do not match experimental observations. An accurate vorticity-flux boundary condition at the orifice, accounting for vorticity generation in the wall boundary layer, is crucial to modelling the dynamics of the unforced jet and ultimately to the study of jet actuation.

This paper seeks a mechanistic understanding of the structure and evolution of vorticity in the transverse jet. Our approach is computational, and our interests are in flows with jet-to-crossflow velocity ratios $r \geqslant 5$, typical of many engineering applications. We focus on the evolution of the jet shear layer issuing from the orifice, in the presence of a thin channel wall boundary layer, by developing a three-dimensional vortex simulation of the transverse jet at large Reynolds number. A local mesh refinement scheme, coupled with a parallel hierarchical method for velocity evaluation (Marzouk & Ghoniem 2005), enables high numerical resolution. Vortex methods provide an attractive framework for simulation of the transverse jet, not least for their explicit link to the formation and dynamics of vortical structures in the flow. Vorticity introduced at the boundary is tracked through the flow field, providing a clear, mechanistic view of its evolution.

The next section (§ 2) offers a more comprehensive overview of the physics of the transverse jet, discussing the structure and dynamics of vorticity in the flow and emphasizing the context of the present contributions. Details of the vortex particle method employed herein are presented in § 3. Boundary conditions for these simulations are developed in § 4; in particular, § 4.2 presents a new formulation of vorticity-flux boundary conditions that account for the interaction of wall boundary layer vorticity with vorticity originating in the jet pipe upstream of the orifice. Results are reported in § 5, where we extract both Lagrangian and Eulerian diagnostics; elucidating the mechanisms that give rise to the vorticity structure of the flow requires connecting both of these viewpoints. Analysis of the flow is thus aided by

examining the evolution of distinguished material structures, instantaneous and time-averaged vorticity isosurfaces, streamlines, and velocity fields. These efforts encompass comparison with previous experiments, analytical studies, and computational results.

2. Physics of the transverse jet

Numerous experiments and computations over the past fifty years have addressed the trajectory, scaling, and structure of jets in crossflow (Margason 1993). In the following, we review some of these results and highlight unresolved areas, providing context for the flow physics explored by our vortex simulations.

2.1. *Flow parameters and coherent structures*

The structure of the flow field is primarily governed by the jet-to-crossflow momentum ratio

$$r = \left(\frac{\rho_j V_j^2}{\rho_\infty U_\infty^2} \right)^{1/2} \tag{2.1}$$

written here as an effective velocity ratio, where ρ_j and V_j are the density and mean velocity of the jet, while ρ_∞ and U_∞ are the density and velocity of the crossflow.

Another controlling parameter is the jet Reynolds number, defined as $Re_j = V_j d/\nu$, where d is the jet diameter and ν is the kinematic viscosity. While only a few studies have discussed the effect of Reynolds number independently of r, it is generally considered to have at best a secondary effect on the large-scale structures of the jet flow field (Kelso *et al.* 1996; Yuan *et al.* 1999). A comparison of experimental results obtained at different Re_j throughout the literature confirms this assertion (Pratte & Baines 1967; Kamotani & Greber 1972). In fact, similarity analyses in Hasselbrink & Mungal (2001*a*) and elswhere invoke Reynolds number invariance, and experimental correlations for the jet trajectory are largely independent of Reynolds number (Margason 1993). Broadwell & Breidenthal (1984) argue that the flame length of the transverse jet – a measure of its mixing rate – is independent of Re_j above a certain critical value, a behaviour typical of free shear flows.

Numerous studies report the presence of large-scale 'coherent' vortical structures in the flow field (Smith & Mungal 1998; Hasselbrink & Mungal 2001*a*). Experimental observations by Fric & Roshko (1994) identify four such structures in the transverse jet: jet shear layer vortices; 'wake vortices' arising from interaction between the jet and the channel wall boundary layer; horseshoe vortices that wrap around the jet exit; and a counter-rotating vortex pair that forms as the jet bends into the crossflow, persisting far downstream.

Jet shear layer vortices result from Kelvin–Helmholtz instability of the cylindrical shear layer shed from the edge of the jet orifice. Kelso *et al.* (1996) report that shear layer roll-up is limited to the upstream side of the jet for smaller Re, while for crossflow Reynolds number $Re_{cf} \equiv U_\infty d/\nu > 1000$ large scale roll-up occurs along the entire perimeter of the shear layer. These structures are analogous to the vortex ring structures typically observed in free jets. Section 5 will characterize the evolution of the jet shear layer in greater detail.

The horseshoe vortices develop close to the wall, wrapping around the nascent column of jet fluid. These vortices form as the wall boundary layer upstream of the jet encounters an adverse pressure gradient and separates (Fric & Roshko 1994; Kelso & Smits 1995; Krothapalli, Lourenco & Buchlin 1990). However, Kelso *et al.* (1996) assert that 'the horseshoe vortex system seems to play only a minor role in the overall

structure' of the transverse jet flow field. Downstream of the orifice, an alternating pattern of upright or 'wake' vortices extends from the wall to the bending jet. These vortices have been studied extensively using various flow visualization techniques (Fric & Roshko 1994; Kelso *et al.* 1996) along with hot-wire anemometry (Rivero, Ferre & Giralt 2001). Fric & Roshko (1994) demonstrate that though the wake vortex pattern is reminiscent of Kármán shedding behind a solid cylinder, its origins are fundamentally different. For larger r, however, the wake structures connecting the wall to the jet fluid are weakened (Smith & Mungal 1998); Fric & Roshko (1994) find that the wake vortices are most orderly at $r = 4$, then diminish in strength as r increases.

For very low r, e.g. $r < 1$, interactions of the jet fluid with the wall boundary layer downstream of the orifice result in a qualitatively different flow structure; this regime is examined in Haven & Kurosaka (1997) for a series of circular, elliptical, and rectangular nozzle geometries and by Andreopoulos & Rodi (1984) for circular jets with $0.5 < r < 2.0$.

The last of the four vortical structures listed above is the counter-rotating vortex pair (CVP). The CVP is a robust feature of the flow over all parameter ranges (e.g. r, Re) and has been a subject of numerous studies (Cortelezzi & Karagozian 2001; Kamotani & Greber 1972; Kelso *et al.* 1996; Lim *et al.* 2001). Broadwell & Breidenthal (1984) argue that the impulse of the jet normal to the crossflow results in a streamwise counter-rotating vortex pair. This argument views the jet as a point source of momentum, and does not address the vorticity transformation mechanisms that actually create the CVP in the near field. (Previous work aimed at understanding these mechanisms is reviewed in § 2.2; we elucidate these mechanisms more fully in § 5.) Though the CVP is present in the mean flow, it has significant unsteady components (Rivero *et al.* 2001) and its instantaneous structure may be strongly asymmetric (Smith & Mungal 1998).

2.2. *Vorticity generation and evolution*

In the absence of body forces, vorticity in a Newtonian barotropic incompressible flow can only be generated at solid boundaries. Large-scale vortical structures detailed in § 2.1 should therefore have their origins in vorticity generated along the crossflow wall and in the boundary layer within the jet nozzle (Fric & Roshko 1994). This link raises a host of interesting and open questions, centring on how vorticity entering the flow is transformed into coherent vortical structures. Vorticity generation is also central to the construction of vorticity-flux boundary conditions, an issue that will be addressed in § 4.2.

In the present work, we focus primarily on the evolution of the jet shear layer and the formation of the counter-rotating vortex pair (CVP). Experimental work by Kelso *et al.* (1996) suggests that the CVP develops in the jet shear layer just above the orifice. Dye visualizations show that the shear layer folds and rolls up near the spanwise edges of the jet; the authors suggest that this folding corresponds to the initiation of the CVP. Simultaneously, Kelvin–Helmholtz instability produces a larger-scale periodic roll-up of the shear layer into ring-like vortices. The upstream parts of these vortex rings tilt as they evolve into the flow, remaining normal to the jet axis. However, Kelso *et al.* (1996) hypothesize that the rings fold such that their downstream parts align with the jet trajectory and contribute to the circulation of the CVP. They also note regular vortex pairing on the upstream side of the shear layer, but observe no pairing on the downstream side.

Lim *et al.* (2001) revisit the near field of the transverse jet with another series of water-tunnel dye visualizations, but offer a different interpretation. They conclude

that there is no evidence of vortex rings in the transverse jet flow field; instead, the cylindrical jet shear layer rolls up to form two independent rows of 'vortex loops', one on the upstream (windward) side and one on the lee side. In this interpretation, 'arms' of both the upstream and lee-side loops contribute vorticity to the CVP, but the overall flow structure does not result from the folding or bending of concentrated vortex rings.

A different mechanism described in Yuan *et al.* (1999) points to quasi-steady 'hanging vortices' formed in the skewed mixing layers on lateral edges of the jet; the authors suggest that these vortices coincide with lateral roll-ups of the shear layer observed by Kelso *et al.* (1996), and that an adverse pressure gradient causes them to break down into a weak CVP. Scalar concentration measurements in Smith & Mungal (1998) indicate that CVP development is delayed with higher r.

The computational study by Cortelezzi & Karagozian (2001), however, lends support to the former 'vortex rings' viewpoint. Using a three-dimensional vortex method, the authors simulate the dynamics of a starting transverse jet. Computational elements take the form of planar axisymmetric vortex filaments introduced above the nozzle edge. By tracking the evolution of these filaments, the authors conclude that the jet shear layer does indeed roll up into vortex rings, which in turn each fold into two sections. In the near field, the downstream section of each ring soon aligns with the jet trajectory, as proposed by Kelso *et al.* (1996). Subsequent evolution of these rings is not clear, however, and conclusions must be tempered by the fact that the computational model introduces only azimuthal vorticity at the nozzle, which we will argue in § 4.2 does not accurately reflect vorticity generation mechanisms in the near field. Finally, it is not clear how closely the start-up dynamics of the jet mirror its mature evolution; simulations end after 3–4 roll-ups of the jet shear layer.

A comparable folding process is shown by Sykes *et al.* (1986), but for material rings introduced into the flow slightly above the jet nozzle. The physical fidelity of these results may be subject to some limitations, namely that the underlying velocity field is steady, obtained from a Reynolds-averaged simulation that allows slip over the crossflow wall and is rather coarse by present standards. Nonetheless, the material rings fold more completely than the vortex rings in Kelso *et al.* (1996) and Cortelezzi & Karagozian (2001), so that material elements originally on the lee and windward sides of the nozzle become nearly coincident on the windward edge of the jet. Interestingly, vortex lines are much shallower than material lines in this simulation, and they contain a significant wall-normal component near the nozzle.

A different approach was taken by Chang & Vakili (1995), who examined the dynamics of individual vortex rings in a crossflow both experimentally and computationally. Rings were found to tilt towards the crossflow (lee sides rising above windward edges) but retain their shapes while translating downstream; weaker rings (i.e. with lower circulation) tilt more sharply than stronger rings. At higher pulsing frequencies, interactions between successive rings disrupted these dynamics. Nonetheless, Hasselbrink & Mungal (2001*a*) argue that an idealized counter-rotating vortex pair must have a constant angle of inclination towards a crossflow and speculate that tilted vortex rings may thus play a role in the far-field structure of the CVP.

While the studies cited above provide valuable characterizations of vorticity dynamics in the transverse jet, less apparent are the mechanisms underlying these dynamics: e.g. why do vortex rings fold, if that is indeed what happens; what causes the initial deformations of the jet shear layer? Coelho & Hunt (1989) address some of these issues with an analytical vortex-sheet model for the near field of the transverse jet. The authors develop an asymptotic solution for the distortion of a

three-dimensional vortex sheet above the jet exit, and argue that interactions between azimuthal and longitudinal components of vorticity on the sheet are essential to predicting its deformation. The jet cross-section deforms in the streamwise direction only when turbulent entrainment is included in the model.

Another unresolved issue is whether the circulation of the counter-rotating vortex pair originates entirely within the jet pipe boundary layer. Water-tunnel flow visualizations by Kelso *et al.* (1996) suggest that the CVP also contains vorticity generated in the channel wall boundary layer. Though the relative magnitude of this contribution must decrease with higher r, it is not clear whether jet vorticity alone is sufficient to characterize the formation and evolution of the CVP. Related questions remain regarding the far-field vortical structure of the jet. Older experimental studies depict the jet's far field as kidney-shaped in cross-section and dominated by the counter-rotating vortex pair, which, once fully developed, persists as far as 1000 diameters downstream (Pratte & Baines 1967). This traditional picture of the jet is based almost entirely on measurements of the mean velocity field (Kamotani & Greber 1972; Fearn & Weston 1974). More recent experiments reveal that instantaneous structure of the far field is significantly more complex. Smith & Mungal (1998) and Yuan & Street (1998) show instantaneous asymmetry of the scalar concentration field at streamwise planes. Yuan *et al.* (1999) show analogous asymmetric contours of streamwise vorticity on downstream planes, dominated by small scales and with significant co-mingling of positive and negative vorticity on both sides of the centreplane. Smith & Mungal (1998) and Zaman & Foss (1997) suggest that even the time-averaged structure of the jet may be asymmetric under certain flow conditions. Rivero *et al.* (2001) contend that mean counter-rotating vorticity is modulated by unsteady coherent vortical structures in the far field, citing a sequence of 'handle-type' vortices that connect to upright vortices in the wake, measured for jets with relatively low velocity ratio, $r = 3.8$. Given the incompletely understood vortical interactions associated with evolution of the jet shear layer and initiation of the CVP, it is not surprising that the far-field structure of the jet should inherit some of this dynamic complexity.

3. Numerical formulation

3.1. *Governing equations*

Equations of motion for inviscid incompressible flow may be written in vorticity transport form, where $\boldsymbol{\omega} = \nabla \times \boldsymbol{u}$:

$$\frac{\mathrm{D}\boldsymbol{\omega}}{\mathrm{D}t} = \boldsymbol{\omega} \cdot \nabla \boldsymbol{u}, \tag{3.1}$$

$$\nabla \cdot \boldsymbol{u} = 0. \tag{3.2}$$

In this Lagrangian description, the right-hand side of (3.1) accounts for stretching and tilting of the vorticity as it is convected by the flow.

Using the Helmholtz decomposition of the velocity field, we write

$$\boldsymbol{u} = \boldsymbol{u}_\omega + \boldsymbol{u}_p \tag{3.3}$$

where $\boldsymbol{u}_\omega$ is the curl of a vector potential and $\boldsymbol{u}_p$ is the velocity of a potential flow ($\boldsymbol{u}_p = \nabla \phi$). It follows from (3.3) that the vector potential and the vorticity are related by a Poisson equation. Given a distribution of vorticity $\boldsymbol{\omega}$, the vortical velocity $\boldsymbol{u}_\omega$

may be recovered from the Biot-Savart law

$$\boldsymbol{u}_\omega(\boldsymbol{x}) = -\frac{1}{4\pi}\int_D \frac{(\boldsymbol{x}-\boldsymbol{x}')\times\boldsymbol{\omega}(\boldsymbol{x}')}{|\boldsymbol{x}-\boldsymbol{x}'|^3}\,\mathrm{d}\boldsymbol{x}' = \boldsymbol{K}*\boldsymbol{\omega}. \tag{3.4}$$

Here $\boldsymbol{K}$ denotes the matrix-valued Biot-Savart kernel.

The above equations are closed by choosing a divergence-free potential velocity field to satisfy a prescribed normal velocity $\boldsymbol{n}\cdot\boldsymbol{u}$ on the boundary of the given domain D:

$$\left.\begin{aligned} \nabla^2\phi &= 0, \\ \boldsymbol{n}\cdot\nabla\phi &= \boldsymbol{n}\cdot\boldsymbol{u} - \boldsymbol{n}\cdot\boldsymbol{u}_\omega \text{ on } \partial D. \end{aligned}\right\} \tag{3.5}$$

Together, (3.1)–(3.5) completely specify the motion of an incompressible inviscid fluid (Chorin & Marsden 1993).

3.2. *Three-dimensional vortex particle methods*

The essence of a vortex method is the discretization of the vorticity field onto Lagrangian computational elements, or particles (Chorin 1973; Leonard 1985; Knio & Ghoniem 1990). In three dimensions, these particles have vector-valued weights $\boldsymbol{\alpha}_i(t) \equiv (\boldsymbol{\omega}\,\mathrm{d}V)_i(t)$ and trajectories $\boldsymbol{\chi}_i(t)$:

$$\boldsymbol{\omega}(\boldsymbol{x}, t) \approx \sum_i^N \boldsymbol{\alpha}_i(t) f_\delta(\boldsymbol{x} - \boldsymbol{\chi}_i(t)). \tag{3.6}$$

The vorticity associated with each element is desingularized with a radially symmetric core function $f_\delta(\boldsymbol{r})$ of radius δ, where $f_\delta(\boldsymbol{r}) \equiv \delta^{-3} f(|\boldsymbol{r}|/\delta)$. The function f must be smooth and rapidly decreasing, satisfying the same moment properties as the Dirac measure up to order $m > 1$ (Beale & Majda 1985).

Given a regularized particle discretization of the vorticity field as in (3.6), the Biot-Savart law (3.4) may be rewritten as follows:

$$\boldsymbol{u}_\omega(\boldsymbol{x}) = \sum_i^N \boldsymbol{K}_\delta(\boldsymbol{x}, \boldsymbol{\chi}_i)\boldsymbol{\alpha}_i \tag{3.7}$$

where the regularized kernel $\boldsymbol{K}_\delta$ results from componentwise convolution with the core function, $\boldsymbol{K}_\delta(\boldsymbol{x}) = \boldsymbol{K} * f_\delta(\boldsymbol{x})$. In the present simulations, we employ the Rosenhead–Moore kernel (Rosenhead 1931; Lindsay & Krasny 2001)

$$\boldsymbol{K}_\delta(\boldsymbol{x}, \boldsymbol{x}') = -\frac{1}{4\pi}\frac{\boldsymbol{x}-\boldsymbol{x}'}{(|\boldsymbol{x}-\boldsymbol{x}'|^2+\delta^2)^{3/2}}\times \tag{3.8}$$

which corresponds to the low-order algebraic core function in Winckelmans & Leonard (1993).

Vortex methods solve the equations of motion via numerical integration for the particle trajectories $\boldsymbol{\chi}_i(t)$ and weights $\boldsymbol{\alpha}_i(t)$. Computing particle trajectories $\boldsymbol{\chi}_i(t)$ requires evaluation of the velocity at each particle at every time step:

$$\frac{\mathrm{d}\boldsymbol{\chi}_i}{\mathrm{d}t} = \boldsymbol{u}(\boldsymbol{\chi}_i). \tag{3.9}$$

Three-dimensional vortex methods also require evaluation of velocity gradients to compute the vortex stretching term and thus the evolution of particle weights. For inviscid flows, ODEs for $\boldsymbol{\alpha}_i(t)$ follow directly from (3.1). The present calculations evaluate vorticity stretch in the context of vortex filaments; this construction is detailed below.

Because convection exactly corresponds to the advection of Lagrangian computational elements, the errors associated with vortex methods contain minimal numerical dissipation (Cottet & Koumoutsakos 2000), rendering these methods well-suited to high-Reynolds-number flows. Also, inherent in the grid-free nature of the method is a dynamic clustering of computational points only where they are needed, i.e. over the small support of the vorticity field.

3.3. *Vortex filament methods*

Consider the evolution of a material line element $\boldsymbol{\delta\chi}$ in a velocity field $\boldsymbol{u}(\boldsymbol{x}, t)$:

$$\frac{\mathrm{D}\boldsymbol{\delta\chi}}{\mathrm{D}t} = \boldsymbol{\delta\chi} \cdot \nabla \boldsymbol{u}. \tag{3.10}$$

Comparing this equation with (3.1), we recall that in inviscid incompressible flows the motion of material lines corresponds to the evolution of vortex lines (Batchelor 1973); a material element coinciding with a vortex line remains on that vortex line for all time.

In a vortex filament scheme, the overall vorticity field is viewed as a collection of vortex filaments; each filament consists of a vorticity field concentrated on a curve $\boldsymbol{r}_j(p)$ that is either closed or extending to infinity. The circulation of each filament is constant at all cross-sections and unchanged as the filament is transported by the flow. From a vortex element point of view, we can discretize the filament along its one-dimensional parameterization, writing

$$\boldsymbol{\omega}_i \, \mathrm{d}V_i = \Gamma_j \boldsymbol{\delta\chi}_i \tag{3.11}$$

where the circulation Γ is indexed by the filament number j. On a given filament, connectivity should be maintained between neighbouring vortex elements. In place of the original discretization in (3.6), we now have

$$\boldsymbol{\omega}(\boldsymbol{x}, t) \approx \sum_j \sum_i^{N_j} \Gamma_j \boldsymbol{\delta\chi}_i(t) f_\delta(\boldsymbol{x} - \boldsymbol{\chi}_i^c(t)). \tag{3.12}$$

Filament methods present several numerical advantages over ordinary three-dimensional vortex particle methods. They preserve fundamental invariants of three-dimensional inviscid flow, e.g. total circulation, impulse, and helicity, and maintain the solenoidal nature of the vorticity field. They also allow efficient evaluation of vorticity stretch: rather than updating $\boldsymbol{\omega}_i \, \mathrm{d}V_i$ explicitly, as in a vortex particle method, one must simply keep track of the deformation of the filament (i.e. $\boldsymbol{\delta\chi}_i(t)$).

It is possible to enforce only a local correspondence between vortex lines and material lines – that is, to initialize vortex elements so that they coincide with specific material lines without requiring that the elements be arranged along continuous closed (or infinite-extent) vortex lines. In this case, we do not have a true filament method; each vortex element may locally coincide with a different vortex line, and thus have a different Γ. However, we can still write $\boldsymbol{\omega}_i \, \mathrm{d}V_i = \Gamma_j \boldsymbol{\delta\chi}_i$ and take advantage of the coincidence of vortex lines and material lines to evaluate vorticity stretch. Discretization of the vorticity field still takes the form of (3.12). In this construction, we refer to the computational elements as lying on 'partial filaments' or 'vortex sticks'. These methods relinquish some of the unique conservation properties of filament methods, but they allow greater flexibility in the initialization of the vorticity.

The present computations describe each filament with a finite set of nodes $\{\boldsymbol{\chi}_i\}_j$. Rather than using these nodes to construct a piecewise linear description of filament

geometry, we use a cubic spline interpolant to describe each space-curve $\boldsymbol{r}_j(p)$ (Ashurst & Meiburg 1988). Curves are parameterized by the accumulated chord length between nodes, and we specify 'not-a-knot' end conditions for the splines (de Boor 1978). The midpoint rule is used for quadrature of the mollified Biot-Savart law along each filament.

Nodes on each filament are advected by the velocity field as specified in (3.9). A second-order predictor/corrector method is used for time integration of these ODEs (Euler predictor, trapezoidal corrector). Two criteria are used for time step control during integration. The first estimates the position error in advecting each node and forces the maximum error estimate, over all the nodes, to be less than some fraction α of the core radius δ. The second criterion requires that each element travel no further than a single core radius over the course of one time step, in effect ensuring that remeshing of the filaments occurs frequently enough to maintain core overlap at all times.

3.4. *Mesh refinement and hairpin removal*

Cubic spline representations for $\boldsymbol{r}_j(p)$ are recomputed from the advected nodes at each time step. As the filaments stretch and fold in response to the strain field of the flow, a mesh refinement scheme must be implemented to ensure core overlap, as well as an adequately detailed description of filament geometry. When $|\delta\boldsymbol{\chi}_i|$ of a given element, as computed from the cubic spline representation, exceeds a given fraction of the core radius, a new node is added at the midpoint of the element, thus splitting the element in two. The location of the new node is also computed from the cubic spline representation: $\boldsymbol{\chi}^{\text{new}} = \boldsymbol{r}(p_{i+1/2})$, and, after advection, the new node is used to compute subsequent spline interpolants.

One result of this mesh refinement scheme is a continual (in fact exponential) growth in the number of vortex elements used to resolve the vorticity field, corresponding to the generation of smaller length scales in the flow. We employ filament-based hairpin removal algorithms to curb the numerical proliferation of small length scales (Chorin 1993). These algorithms directly remove small-scale folds in vortex lines (i.e. 'hairpins'), yet have been demonstrated to preserve the dynamical characteristics of large-scale vortical structures and to conserve integral quantities of the flow, such as kinetic energy and linear impulse (Chorin 1993). By considering the statistical mechanics of vortex filaments at the inviscid limit, hairpin removal can be justified as a renormalization procedure (Chorin 1994; Chorin & Hald 1995; Chorin 1996).

Hairpins are identified by computing the angle between adjacent vortex elements; for simplicity, we use the chords between neighbouring nodes to compute these angles. When the angle exceeds a certain maximum, given by the parameter $(\cos\theta)_{\min}$, the pair of elements is replaced by its vector sum. Additional rules are applied to deal with adjacent hairpins on a single filament. Our current implementation does not search for hairpins between elements on different filaments; therefore, explicit filament splitting and reconnection as described by Chorin (1993) are not pursued.

In addition to splitting elements and removing hairpins, we merge small elements with their neighbours along a filament if the linear extent of the element becomes too small, e.g. for $|\delta\boldsymbol{\chi}_i| < 0.2\delta$. In practice, we find that hairpin removal is significantly more important than small-element merging in curbing the proliferation of vortex elements and in regularizing filament geometry.

3.5. *Parallel implementation*

The present computations are implemented on a massively parallel distributed-memory computer using message passing, via the standard MPI libraries. The bulk of

the computational time is spent evaluating the vortical velocity field on every filament node. To speed evaluation of this N-body problem, we use an adaptive treecode developed by Lindsay & Krasny (2001). Parallel implementation of this treecode, or indeed of any hierarchical solver, presents a number of computational and geometric challenges. We employ clustering algorithms for parallel domain decomposition in this context, as well as new heuristics for dynamic load balancing. Marzouk & Ghoniem (2005) and Marzouk (2004) present this development in detail.

An efficient scalable parallel implementation enables vortex simulations with large numbers of elements, which are necessary for high resolution and for continuing the evolution of the jet long enough in time to distinguish between startup transients and mature dynamics. Simulations reported in this paper contain as many as 3.5×10^6 vortex elements.

4. Boundary conditions

We now discuss boundary conditions particular to the simulation of the transverse jet flow field, both normal-velocity boundary conditions and vorticity flux boundary conditions. In the expressions below, all variables are made dimensionless by d, the jet diameter, and U_∞, the velocity of the uniform crossflow. The crossflow is directed in the positive x-direction; the jet centreline is aligned with the y-axis; and the z-axis is in the spanwise direction. Except on the disk of the jet orifice, the (x, z)-plane is taken to be a solid wall through which we enforce a no-normal-flow boundary condition.

4.1. *Normal-velocity boundary conditions*

The jet outflow is represented by a semi-infinite cylindrical vortex sheet of radius $1/2$ extending from $y = 0$ to $y = -\infty$, with strength $\boldsymbol{\gamma} = 2r\hat{\boldsymbol{e}}_\theta$ where $\hat{\boldsymbol{e}}_\theta$ is the tangential unit vector in the (x, z)-plane. The vorticity in this cylinder is mollified by a core function identical to that used with the computational vortex elements. This matching is crucial. An unmollified cylindrical vortex sheet, or, equivalently, a uniform distribution of potential sources over the jet orifice with surface source strength $2r$, yields a singularity in the radial velocity at the nozzle edge when paired with the computational vortex elements. This singularity was noted, but left uncorrected, in Cortelezzi & Karagozian (2001). We discretize the vortex sheet using vortex particles with core radius, axial spacing, and azimuthal spacing identical to the vortex particles introduced into the flow, as shown in figure 1.

The crossflow velocity is given by the potential $\phi_\infty = x$. Image vortex elements are used to model the behaviour of vorticity in the semi-infinite domain, i.e. to enforce no-flow through the channel wall $y = 0$. Writing the vorticity in the domain componentwise $\boldsymbol{\omega} = (\omega_x, \omega_y, \omega_z)$, the image vorticity has components $\boldsymbol{\omega}_{\text{img}} = (-\omega_x, \omega_y, -\omega_z)$.

4.2. *Boundary generation of vorticity*

Vorticity produced in the jet boundary layer (i.e. in the pipe below the $y = 0$ plane) is represented by a single sheet of azimuthal vorticity. Introducing this vorticity into the flow every Δt_{noz} time units, we divide it among n_θ vortex elements distributed along the edge of the jet nozzle, where $\Delta\theta = 2\pi/n_\theta$. These elements have weight

$$(\boldsymbol{\omega}_i \, \mathrm{d}V_i)_o = -\frac{r^2}{4} \Delta t_{noz} \Delta\theta \hat{\boldsymbol{e}}_\theta. \tag{4.1}$$

In employing a single sheet of vortex elements, we elect not to resolve the distribution of vorticity within the jet boundary layer. In this construction, the thickness of the jet boundary layer is essentially controlled by the core size δ.

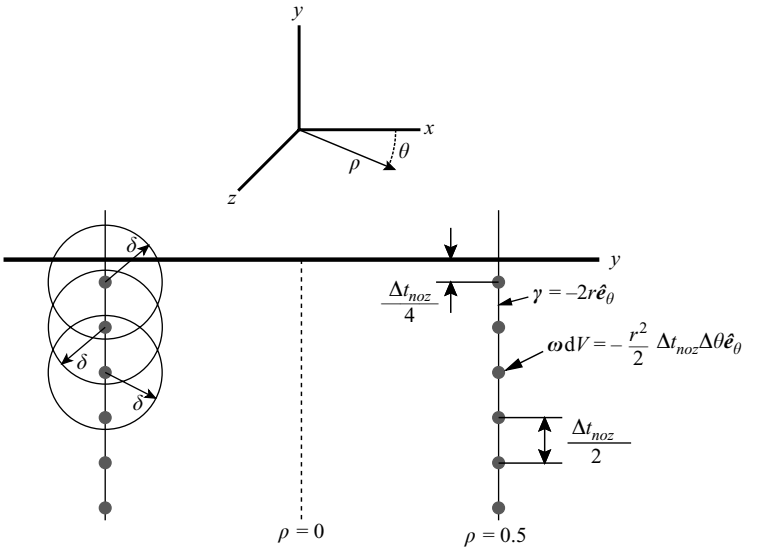

FIGURE 1. Discretization of the cylindrical vortex sheet representing the jet outflow for $y > 0$.

Azimuthal vorticity alone does not provide a complete picture of the jet near field, however. In figure 2(*a*), we show a vortex simulation of the transverse jet performed at $r = 7$, introducing purely azimuthal vorticity at the jet orifice as expressed in (4.1), with numerical parameters given in § 5.1. The upper half of the figure shows the instantaneous velocity field on the $y = 0$ plane at $\tilde{t} = 2.40$, a time by which the near field has settled to a stationary envelope. The lower half of the figure is a plan view of streamlines originating at $y/d = 0.5$, $x/d = -1.4$ and terminating on the $y/d = 1.8$ plane. Streamlines take a shallow path around the jet; the streamlines closest to the centreplane penetrate well into the circular jet boundary. In addition, figure 2(*a*) shows a streamwise component of velocity that is substantially amplified on the jet orifice. This behaviour contrasts with visualizations of the near-wall flow by Fric & Roshko (1994) for transverse jets with $r = 4$–10. Figure 3 reproduces these results at $r = 8$. Smoke is released from a rake of wires upstream of the orifice at $y/d = 0.5$, and the resulting streaklines curve around the jet column without penetrating it. We intend only a qualitative comparison here, focused on the windward side of the jet exit where the flow at $y/d = 0.5$ is nearly steady. In this region, streamlines in figure 2 should bear a strong similarity to Fric & Roshko's streaklines – that is, they should not penetrate the jet boundary. Anticipating our arguments below, we note that a velocity field in which the crossflow flows mostly around the jet column is kinematically consistent with the presence of wall-normal vorticity at the interface.

Moreover, the velocity field in figure 2(*a*) and its accompanying near-wall streamlines suggest a larger impact on the entire near-field jet trajectory, borne out in figure 4(*a*). This figure shows instantaneous velocity vectors and streamlines on the centreplane $z = 0$, again from an $r = 7$ simulation that introduces only azimuthal vorticity at the nozzle edge. The jet is angled downstream from the vertical. This initial trajectory is at odds with instantaneous particle image velocimetry (PIV) measurements by Hasselbrink & Mungal (2001*b*), analytical predictions of the initial trajectory by Coelho & Hunt (1989), flow visualizations by Lim *et al.* (2001) (e.g. figure 12 in this paper), and many other observations of the near field (e.g. Kelso *et al.* 1996). In the light of these studies, the behaviour in figures 2(*a*) and 4(*a*) appears unphysical.

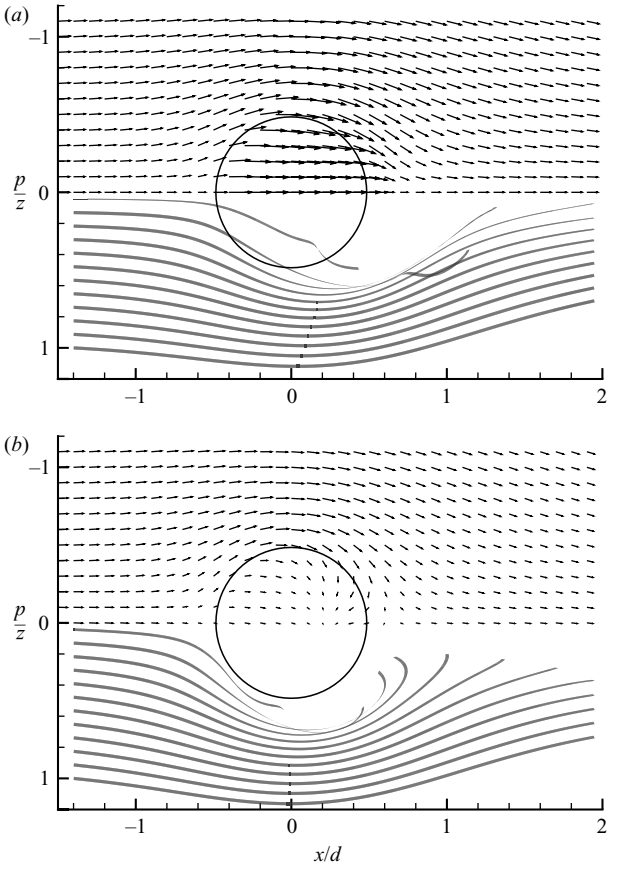

FIGURE 2. Velocity vectors on the $y/d = 0$ wall (upper half) and a plan view of streamlines originating at $y/d = 0.5$ (lower half). (*a*) Azimuthal vorticity only, (*b*) full vorticity flux boundary condition, at $\tilde{t} = 2.40$, $r = 7$. Streamlines are terminated on a horizontal plane $1.8d$ above the jet exit.

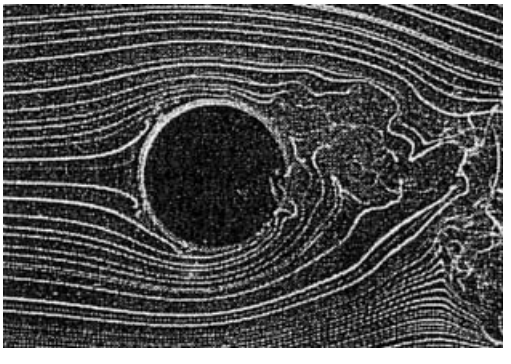

FIGURE 3. Flow above the orifice of a transverse jet at $r = 8$, visualized with smoke streaklines injected at $y/d = 0.5$. Crossflow is directed from left to right. Reproduced from Fric & Roshko (1994).

We appeal to first principles to quantify the wall-normal vorticity flux, but first make the focus of the present formulation clear. Upstream of the jet, vorticity produced in the channel wall boundary layer initially points in the negative spanwise $(-\hat{z})$

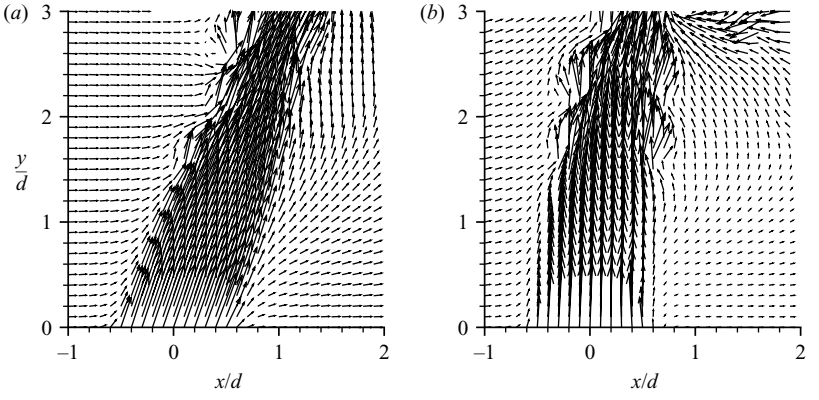

FIGURE 4. Velocity field on the centreplane $z=0$ at $\tilde{t}=2.40$, comparing two vorticity-flux boundary conditions: (*a*) azimuthal vorticity only, (*b*) full vorticity flux boundary condition.

direction. Our interest lies in the interaction of this vorticity with the jet flow at the separation line surrounding the nozzle edge; in particular, we wish to model channel wall vorticity in the jet–crossflow interface at $y=0$. This vorticity is carried upward by the jet (Fric & Roshko 1994) and may thus affect the jet trajectory and evolution over the range of r. Our simulations are essentially inviscid, and thus we do not consider growth of the wall boundary layer or separation events away from the jet nozzle, as these have a diminishing role in determining jet dynamics for larger r, e.g. $r \geqslant 4$ (Fric & Roshko 1994). Nor do we explore a range of boundary layer thicknesses δ_{bl}/d (Muppidi & Mahesh 2005). Instead we represent the total circulation per unit length in the boundary layer, where a meaningful thickness parameter is simply the element core size δ, here equal to $0.1d$. Our formulation is therefore in the regime of a thin boundary layer ($\delta_{bl}/d \ll 1$) that remains attached to the channel wall until interacting with the jet flow.

By considering the slip of crossflow velocity over the edge of the jet orifice, or, alternatively, the penetration of crossflow velocity into the jet fluid at the wall, we now derive modifications to the vortex element strengths given in (4.1). These modifications, due to channel wall boundary layer vorticity, are $O(r)$ rather than $O(r^2)$.

First, consider the slip of crossflow velocity over the edge of the jet orifice. In polar coordinates (ρ, θ) centred at the origin of the (x, z)-plane, the radial (ρ) component of this slip velocity is cancelled locally by an azimuthal vortex sheet of strength $\boldsymbol{\gamma} = -\cos\theta\hat{\boldsymbol{e}}_\theta$. These vortex sheets are shed a distance $r\Delta t_{noz}/2$ into the flow every time step. Again dividing this vorticity over $n_\theta = 2\pi/\Delta\theta$ elements distributed along the nozzle edge, we obtain

$$(\boldsymbol{\omega}_i \mathrm{d}V_i)_1 = -\frac{r}{4}\cos\theta_i \Delta t_{noz}\Delta\theta\hat{\boldsymbol{e}}_\theta \tag{4.2}$$

for the vortex element strengths due to this interaction.

Next we observe that the azimuthal component of the crossflow velocity does not penetrate into the jet at $y=0$. This requires a discontinuity of azimuthal velocity across the interface, which corresponds to a vortex sheet of strength $\boldsymbol{\gamma} = \sin\theta\hat{\boldsymbol{e}}_y$. Thus the interaction of crossflow vorticity with the jet results in wall-normal vorticity; this idea is confirmed heuristically by considering the tilting of a spanwise material line that encounters either spanwise extremity of the jet. Again, we expect these vortex sheets to be shed at the local flow velocity, i.e. $r\Delta t_{noz}/2$ every time step. Dividing the

vorticity over elements along the nozzle edge, we obtain element strengths as

$$(\boldsymbol{\omega}_i \, \mathrm{d}V_i)_2 = \frac{r}{4} \sin\theta_i \Delta t_{noz} \Delta\theta \hat{\boldsymbol{e}}_y. \tag{4.3}$$

Note that the vorticity strengths in (4.3) reflect a slip velocity of $\sin\theta\hat{\boldsymbol{e}}_\theta$, not $2\sin\theta\hat{\boldsymbol{e}}_\theta$ as in two-dimensional flow around a cylinder with unit free-stream velocity. The transverse jet near field thus differs from flow around a solid cylinder not only in its mechanisms of vorticity generation but in the resulting magnitude of wall-normal vorticity along the interface.

A final constraint arises from kinematic considerations. In cylindrical coordinates, for vorticity confined to a sheet emanating from the nozzle edge, the solenoidality constraint on the vorticity field $\nabla\cdot\boldsymbol{\omega} = 0$ requires

$$\frac{\partial\omega_y}{\partial y} = -2\frac{\partial\omega_\theta}{\partial\theta}. \tag{4.4}$$

Each new set of vortex elements represents vorticity in the flow for $0 < y < r\Delta t_{noz}/2$. We thus introduce elements so that their centers lie at $y = r\Delta t_{noz}/4$. Summing jet and channel-wall boundary layer contributions to vortex element strengths and enforcing (4.4), we obtain the following expression for the total strength of the vortex elements introduced at each time step:

$$\boldsymbol{\omega}_i \mathrm{d}V_i = \left(-\frac{r^2}{4} - \frac{r}{4}\cos\theta_i\right)\Delta t_{noz}\Delta\theta\hat{\boldsymbol{e}}_\theta + \left(\frac{r}{4}\sin\theta_i - \frac{r^2\Delta t_{noz}}{8}\sin\theta_i\right)\Delta t_{noz}\Delta\theta\hat{\boldsymbol{e}}_y. \tag{4.5}$$

Using this new vorticity-flux boundary condition, we perform another vortex simulation of the transverse jet at $r = 7$, again with numerical parameters detailed in § 5.1. The resulting near-wall velocity field is depicted in figure 2(*b*). Streamlines originating in the crossflow at $y/d = 0.5$ curve more sharply around the jet and converge toward the centreplane downstream of the orifice. Streamlines closer to the lee side of the orifice are lifted upwards into the complex vortical structures of the jet and thus appear somewhat irregular in plan view. Comparing velocity vectors on the $y/d = 0$ plane with those in figure 2(*a*), we find that the streamwise velocity on the orifice is diminished by a factor of 5–7. Focusing on the windward side of the orifice, qualitative correspondence with the flow visualization in figure 3 is much improved.

These differences extend to the velocity field on the centreplane, where the impact of boundary conditions is even more dramatic. Figure 4(*b*) shows instantaneous velocity vectors and streamlines on the $z = 0$ plane at $\tilde{t} = 2.40$ and $r = 7$, again obtained with the full vorticity-flux boundary condition. Comparing figures 4(*a*) and 4(*b*) clearly illustrates the effect of nozzle-edge vorticity on the near-field trajectory of the jet. Neglecting vorticity in the channel wall boundary layer results in a jet immediately angled downstream, inconsistent with experimental observation. Modelling the interaction of channel wall vorticity with the jet, however, results in a jet issuing more vertically from the orifice, consistent with the many investigations cited above.

It is worthwhile to contrast the present vorticity formulation with other computational vortex models of the transverse jet. Our earliest computational effort (Marzouk & Ghoniem 2002) neglected vorticity in the crossflow boundary layer, focusing only on the evolution of jet azimuthal vorticity. Shortcomings of this approximation are those detailed above. The vortex simulation by Cortelezzi & Karagozian (2001) also introduces filaments carrying only azimuthal vorticity, but enforces a no-slip boundary condition along the channel wall by modifying the uniform crossflow with a cubic boundary layer profile. This boundary layer profile

corresponds to a finite spanwise vorticity distributed along the normal to the wall; yet this vorticity is not represented by vortex elements, nor is it allowed to evolve. Such a representation of the channel wall boundary layer is inconsistent with the Helmholtz decomposition (3.3), and thus with the equations of motion (3.1)–(3.5). Trajectories in the present work, which account for vorticity generation in a thin boundary layer along the wall, appear more upright than in Cortelezzi & Karagozian (2001), despite attempts at varying the thickness of imposed boundary layer profile in the latter.

5. Results and discussion

We now present the results of vortex simulations of the spatially evolving transverse jet, at velocity ratios r ranging from 5 to 10. Analysis of the flow is aided by extracting and examining the evolution of material lines carrying vorticity, instantaneous and averaged vorticity isosurfaces, streamlines, and trajectories. We will also examine the impact of the vorticity flux boundary conditions derived in the previous section and develop analytical expressions for the near-field vortex lines.

5.1. *Numerical parameters*

Numerical parameters for the vortex simulations were chosen as follows: Overall spatial resolution is governed by the core radius δ, chosen to be 0.1. The number of elements discretizing vorticity introduced along the nozzle edge (e.g. the initial azimuthal resolution) is $n_\theta = 64$. Axial resolution depends on the time step between successive filament introductions, Δt_{noz}. We keep the distance $r\Delta t_{noz}$ relatively constant for different choices of r. Thus, for the $r = 7$ jet we put $\Delta t_{noz} = 0.01$; for $r = 10$ we put $\Delta t_{noz} = 0.0075$; and for $r = 5$ we put $\Delta t_{noz} = 0.0125$.

The length threshold for splitting elements is fixed at 0.9δ, while the length threshold for merging small elements along a filament is 0.2δ. We fix the cutoff for hairpin removal at $(\cos\theta)_{\min} = 0$. The error tolerance parameter α controlling the integration time step in § 3.3 is set to 0.01.

A series of numerical convergence studies were performed to justify the above choices of numerical parameters. The trajectories, vortical structures, and dynamical processes reported below were preserved under further refinement of the spatial resolution parameters δ, n_θ, and Δt_{noz}, suggesting that the present simulations are well-resolved at the chosen values. Filament geometries were observed to be unaffected by further reduction of the error tolerance parameter α. Similarly, the jet trajectory as well as the shape and location of large-scale vortical structures in the flow were not affected by relaxation of the hairpin removal cutoff $(\cos\theta)_{\min}$, evidence that results reported below are insensitive to the hairpin removal process.

For a given set of numerical parameters, the number of computational elements resolving the vorticity field grows steadily over the course of a simulation; this growth is an explicit consequence of the mesh refinement scheme (§ 3.4) and the continual introduction of new vorticity at the nozzle.

5.2. *Vorticity transformation mechanisms*

5.2.1. *Vortex filament evolution*

We first examine successive snapshots of computational vortex filaments in transverse jets at various jet-to-crossflow velocity ratios r. Figure 5(*a–e*) shows filaments in three-dimensional perspective for the $r = 7$ jet. Times $\tilde{t}$ corresponding to each snapshot are normalized by d/U_∞, the crossflow convective time scale. These snapshots span the computed evolution of the $r = 7$ jet. Figure 6 shows analogous snapshots for

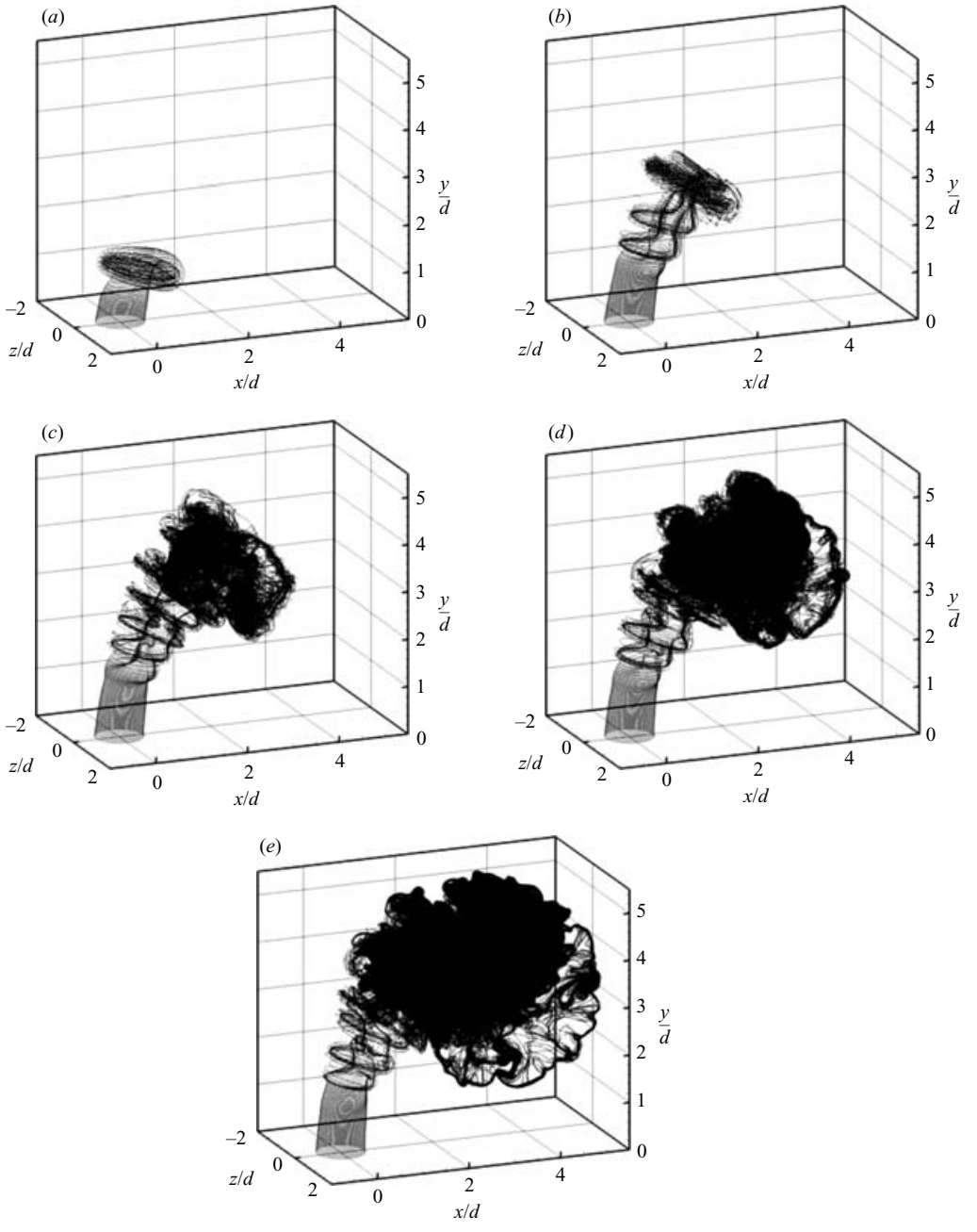

FIGURE 5. Perspective view of vortex filaments in the evolving transverse jet at five successive times, for $r = 7$. (*a*) $\tilde{t} = 0.60$, (*b*) $\tilde{t} = 1.20$, (*c*) $\tilde{t} = 1.80$, (*d*) $\tilde{t} = 2.10$, (*e*) $\tilde{t} = 2.40$.

the $r = 5$ and $r = 10$ jets, towards the end of their computed evolutions. Figure 6 also illustrates the r-dependence of jet evolution at identical jet convective times $t/(d/rU_\infty)$.

Several important features are apparent in these figures. The most obvious is that the jet penetrates more deeply into the domain for larger r. The envelope of the

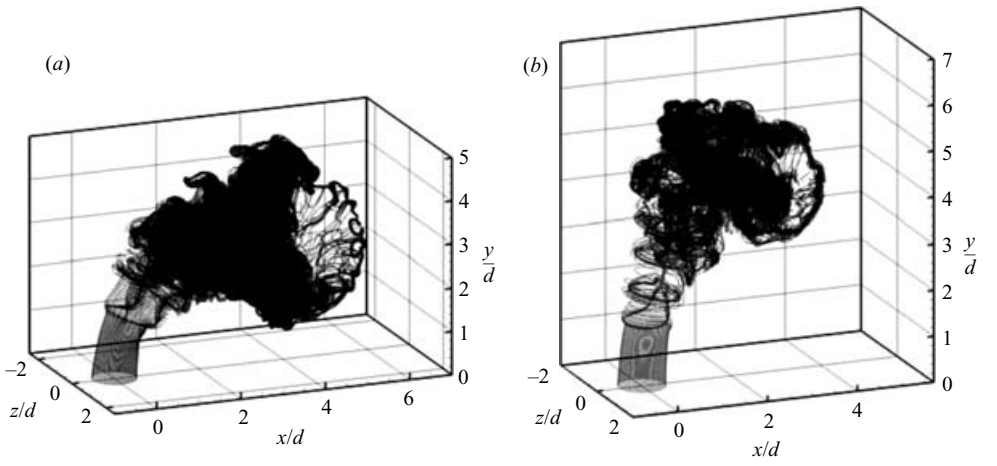

FIGURE 6. Perspective view of vortex filaments in the transverse jet for (*a*) $r = 5$, $\tilde{t} = 3.00$ and (*b*) $r = 10$, $\tilde{t} = 1.50$.

$r = 10$ jet is more upright than that of the $r = 7$ and $r = 5$ jets, and although all the jets are deflected by the crossflow in the positive x-direction, the larger-r jet begins significant tilting much later in its evolution – later in the sense of both jet convective time and wall-normal distance y/d.

Next, all three cases show roll-up of the jet shear layer, indicative of the expected Kelvin–Helmoltz instability. Shear layer roll-up is indicated by the axial grouping together of vortex filaments and is particularly visible on the upstream (windward) side of the jet. On the lee side of each jet, a more complex out-of-plane distortion of the vortex filaments accompanies the roll-up. This distortion holds the key to the development of counter-rotating vorticity and will be explored more fully in the next subsection. As the jets evolve further, filaments stretch and fold in response to flow strain and are continually remeshed with a growing number of nodes. At all values of r, large-scale vortical structures undergo a critical transition at the head of each jet, breaking up to form a 'mushroom cloud' dominated by complex shorter-length-scale vortical interactions. This transition is accompanied by more pronounced bending into the crossflow.

We also note that, though the jets continue to evolve downstream, the near-field envelope of each jet seems to mature. Comparing figure 5(*d*) and figure 5(*e*), for instance, the jet envelope seems unchanged for $x/d < 2.0$. At this stage, the initial orientation of the jet is normal to the wall for all three values of r.

5.2.2. *Shear layer folding and counter-rotating vorticity*

The out-of-plane distortion of vortex filaments may be analysed more carefully by following the evolution of individual segments of the jet shear layer. Consider first the $r = 7$ jet: we count nine distinct roll-up events on the windward side of the jet as it evolves from $\tilde{t} = 0$ to $\tilde{t} = 2.60$. The fate of the ring-like vortical structures formed in the first two roll-ups differs qualitatively from that of subsequent structures. This is not surprising, as the earlier structures interact with a very different vorticity field than do later ones. In the mature transverse jet, the emerging shear layer is stretched and deformed by existing vorticity, producing vortical structures that in turn have an impact on the evolution of subsequent vorticity.

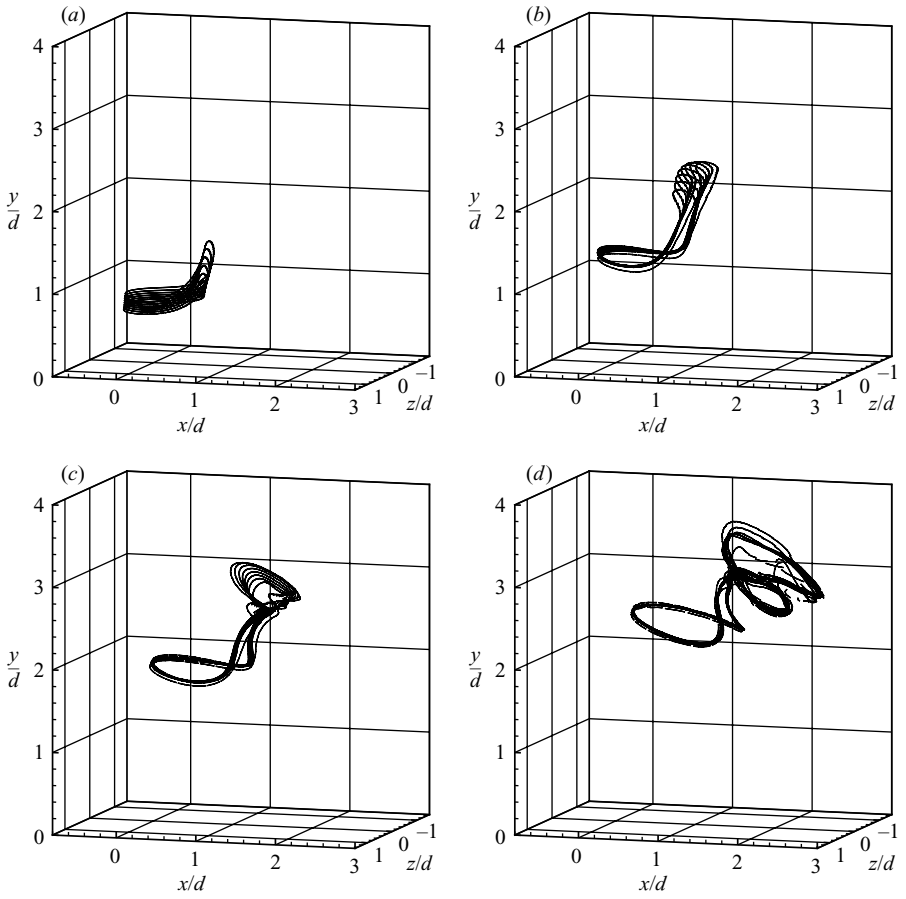

FIGURE 7. Shear layer folding in the transverse jet, for $r = 7$. Snapshots follow the evolution of vortex elements introduced for $\tilde{t} \in [0.45, 0.52]$, corresponding to the second shear layer roll-up. (*a*) $\tilde{t} = 0.72$, (*b*) $\tilde{t} = 0.92$, (*c*) $\tilde{t} = 1.12$, (*d*) $\tilde{t} = 1.32$.

Let us examine this process step-by-step, remaining focused on the $r = 7$ jet. The first roll-up, occurring at the head of the shear layer in figure 5(*a*), gives rise to a vortex ring that remains strong in the flow for subsequent times. For instance, this ring can be seen near the head of the jet in figure 5(*b*), $\Delta\tilde{t} = 0.60$ later, though it has pulled additional vorticity through its centre. The ring stays relatively planar as it tilts into the crossflow, inducing deformations of the vorticity-carrying material around it that contribute to the complicated structure downstream.

Next, in figure 7 we show only those vortex elements that were introduced between $\tilde{t} = 0.45$ and $\tilde{t} = 0.52$. As detailed in § 3, elements take the form of locally defined vortex filaments or 'sticks'. Upon introduction, though these elements primarily carry azimuthal vorticity, they actually contain multiple components of vorticity whose initial strengths vary along the azimuthal coordinate in accordance with (4.5). The filaments grow in length and are remeshed independently of each other in response to flow-induced stretch. Their initial arrangement, however, is essentially around a ring, and the filaments collectively maintain this coherence as they evolve. Thus it is meaningful to speak of the geometric transformations of a vorticity-carrying material ring, i.e. a shear layer segment, when describing the collective evolution of this group

of vortex elements. These material rings will not typically become coherent vortex rings, as detailed below.

The segment of the shear layer shown in figure 7, initially planar, participates in the second roll-up on the windward side of the $r = 7$ jet. But the evolution of the entire material ring is significantly more complex. This evolution is traced in figure 7(*a–d*) with four snapshots, equally spaced in time. The shear layer first deforms out-of-plane, as shown in figure 7(*a*); here, the downstream (lee) side of the shear layer has stretched upwards to form a tongue-like structure. This deformation can be attributed to velocity induced by the preceding vortex ring; above and slightly downstream of the filaments shown, the first ring induces an upward velocity on the lee side of the ensuing shear layer. In figure 7(*b*), the tongue-like structure becomes more pronounced and the filaments group together; the shear layer is rolling up, and the roll-up centres on the filaments we have selected here. At the very top of the tongue-like structure, however, a new deformation is present: vortex elements are curving towards the windward side of the jet. Vertical arms of the tongue-like structure carry counter-rotating vorticity, pointing upwards for $z > 0$ and downwards for $z < 0$. Material elements between the counter-rotating arms are transported backwards (in the negative x-direction), normal to the vorticity. As the ring evolves further, its upper portion flattens and the entire structure takes the form of two vortex arcs connected by vertical arms. While the arms are approximately aligned with the jet trajectory in figure 7(*c*), they curve against the crossflow in figure 7(*d*); this final stage of deformation is unique to the second shear layer segment, due to interactions with the first vortex ring, and is not repeated as the jet near field matures.

Subsequent segments of the shear layer undergo a series of deformations reminiscent of those just described, but settle into a repeating pattern. This pattern may be summarized by tracing the evolution of two complementary groups of elements. Figure 8 is representative of the first group, showing vortex elements introduced into the flow between $\tilde{t} = 1.09$ and $\tilde{t} = 1.14$, in four successive snapshots each separated by $\Delta\tilde{t} = 0.20$. The start of upward deformation on the lee side of the shear layer is shown in figure 8(*a*). Upward deformation becomes more pronounced in figure 8(*b*). In contrast to the shear layer segment considered in the preceding paragraph, it is the lee side of the present shear layer segment that rolls up most strongly; the windward side remains sheet-like. Vertical arms form below the lee-side roll-up on either side, but their length is at most one diameter. As with the earlier tongue-like structure, the vertical arms carry counter-rotating vorticity essentially aligned with the jet trajectory. In figure 8(*c*) the lee-side roll-up begins curving towards the windward side of the jet; at this stage, the lee-side roll-up is a vortex arc in its own right. Deformation of this arc is consistent with the orientation of the counter-rotating vorticity; it is probably the result of velocity induced both by counter-rotating vorticity on the present vertical arms (i.e. below the roll-up) and by counter-rotating vorticity produced by earlier segments of the shear layer (not shown in these figures but situated above the roll-up). (Coupling between successive shear layer segments is explicitly discussed below.) Figure 8(*d*) shows that the lee-side vortex arc has curved more completely towards the windward boundary of the jet while the rest of the shear layer segment's vorticity has become somewhat more convoluted. Note that the vortex arc carries vorticity pointing in the negative z-direction, opposite in sign to the vorticity that has remained on the windward side of the shear layer segment.

Figure 9 is representative of the second group of vortex elements. This figure traces the evolution of the shear layer segment immediately following that of figure 8; its elements were introduced into the flow between $\tilde{t} = 1.16$ and $\tilde{t} = 1.22$. This shear layer

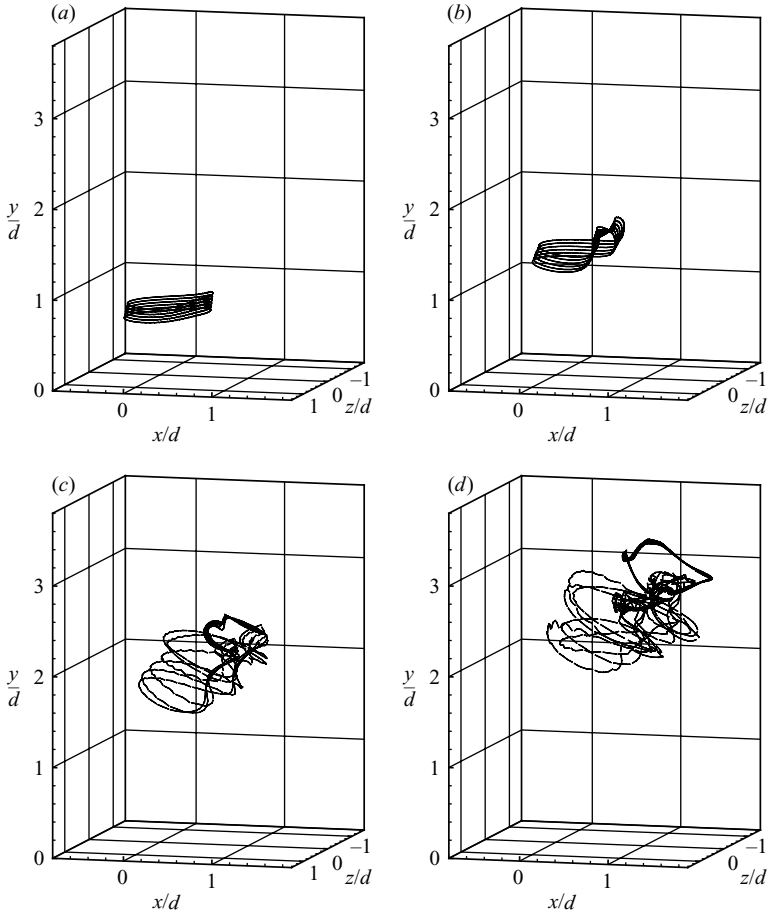

FIGURE 8. Shear layer folding in the transverse jet, for $r = 7$. Snapshots follow the evolution of vortex elements introduced for $\tilde{t} \in [1.09, 1.14]$, corresponding to the sixth lee-side roll-up. (*a*) $\tilde{t} = 1.34$, (*b*) $\tilde{t} = 1.54$, (*c*) $\tilde{t} = 1.74$, (*d*) $\tilde{t} = 1.94$.

segment is also pulled upwards on its lee side, as shown in figure 9(*a*), but it rolls up most strongly on its windward side. This shear layer segment in fact participates in the sixth roll-up on the windward side of the jet. Now it is the lee side that, though deformed out-of-plane, remains more sheet-like, see figure 9(*b*). Vertical arms of counter-rotating vorticity still develop as the lee side is pulled upwards, however. The arms themselves show a tight grouping of vortex elements, clearly visible in figure 9(*c*); these rolled-up vertical arms coincide with the vertical arms in the first group, in figure 8. Figure 9(*c*) shows that lee-side elements still get swept towards the windward boundary of the jet, but without undergoing roll-up. Lee-side elements appear slightly more disorganized in figure 9(*d*); some of the elements seem to be winding around the primary vertical arms.

Shear layer segments in both groups thus exhibit strong similarities in their evolution. Each segment transforms into two arcs contributing opposite senses of vorticity to the jet's windward boundary and connected by vertical arms of counter-rotating vorticity. The two groups differ in whether it is the lee side or the windward side of the shear layer that rolls up more strongly. Moreover, the two shear layer

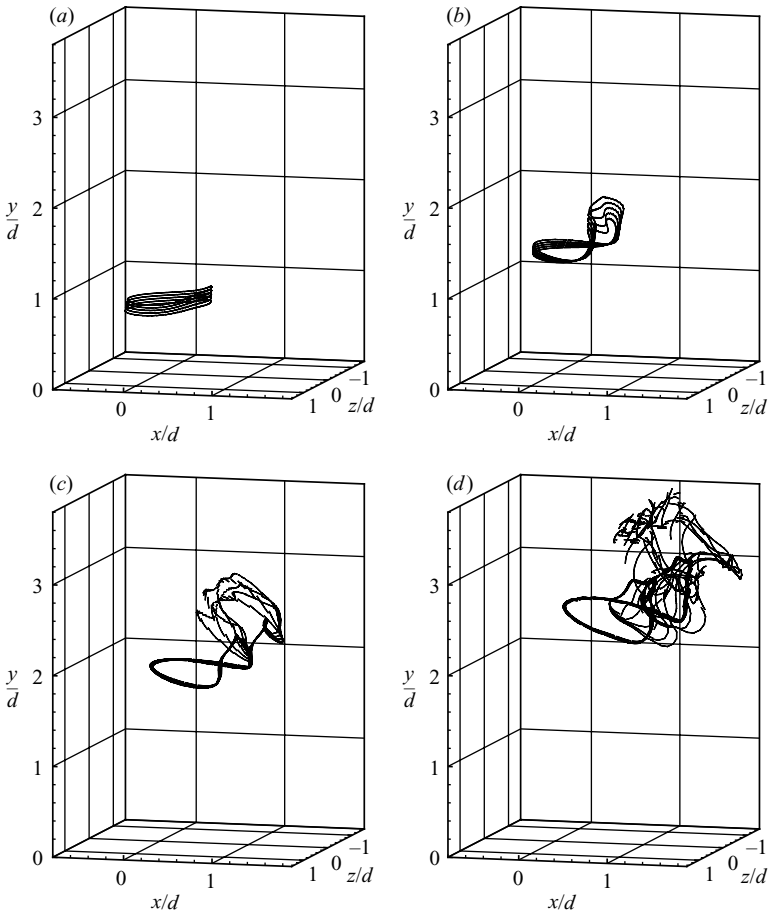

FIGURE 9. Shear layer folding in the transverse jet, for $r = 7$. Snapshots follow the evolution of vortex elements introduced for $\tilde{t} \in [1.16, 1.22]$, corresponding to the sixth windward-side roll-up. (*a*) $\tilde{t} = 1.42$, (*b*) $\tilde{t} = 1.62$, (*c*) $\tilde{t} = 1.82$, (*d*) $\tilde{t} = 2.02$.

segments we selected are complementary because they coincide in space after their transformations are complete. In other words, the upper vortex arc of the first group is surrounded by disorganized elements of the second group, and the lower vortex arc of the second group is surrounded by disorganized windward-side elements of the first. Figure 10 explicitly illustrates this configuration. Figure 10(*a*) shows the two successive segments of the shear layer at $\tilde{t} = 1.56$, before significant deformation has occurred. The segments are colour-coded; the grey segment is the first group of vortex elements analysed above, while the red segment is the second group. Now consider the geometry of these shear layer segments at $\tilde{t} = 2.00$, shown in figure 10(*b*). It is clear that the transformed shear layer segments coincide in space, with group 1 contributing to the lee-side roll-up and group 2 contributing to the windward roll-up.

These observations are consistent with flow visualizations by Lim *et al.* (2001) that reveal distinct lee-side and windward-side 'vortex loops', reproduced in figure 12 for an $r = 4.6$ jet. In shape and in location, these vortex loops correspond to the lee-side and windward-side roll-ups identified above. Lim *et al.* (2001) contend that the two types of vortex loops do not result from the folding of coherent vortex rings, and our simulations support their interpretation. In the mature transverse jet (after the

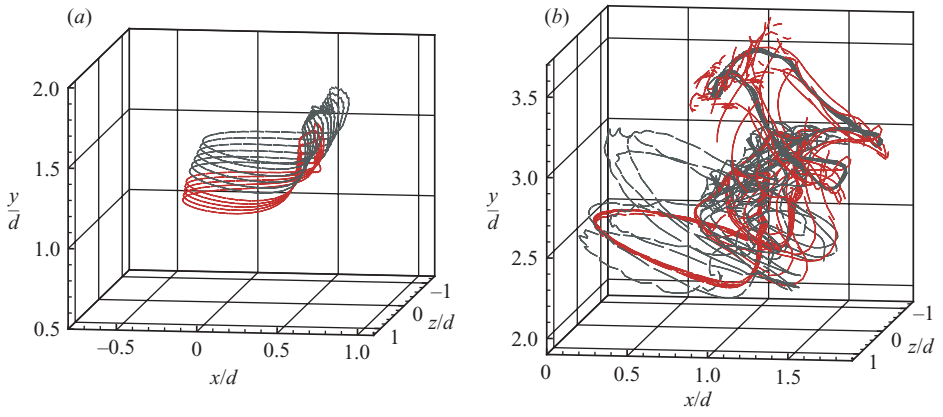

FIGURE 10. Combined evolution of two successive shear layer segments in the $r = 7$ jet at (*a*) $\tilde{t} = 1.56$, (*b*) $\tilde{t} = 2.00$. Vortex elements in grey match those in figure 8 and in (*b*), contribute to a lee-side roll-up. Vortex elements in red match those in figure 9 and in (*b*), contribute to a windward-side roll-up.

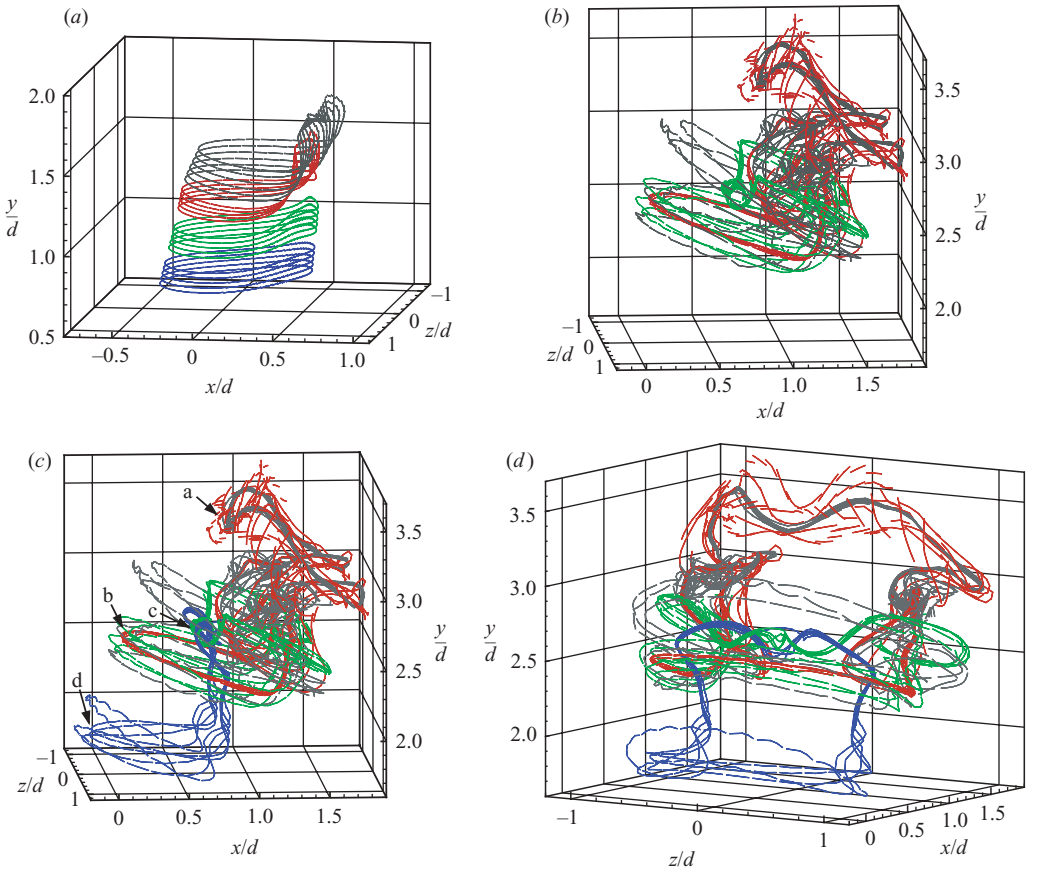

FIGURE 11. Interlocking structure of four folded shear layer segments, $r = 7$. Grey and red segments are identical to those shown in figure 10. (*a*) Groups 1, 2, 3, and 4, $\tilde{t} = 1.56$. (*b*) Groups 1–3, $\tilde{t} = 2.00$. (*c*) Groups 1–4 $\tilde{t} = 2.00$; labels identify roll-ups discussed in the text. (*d*) Groups 1–4, $\tilde{t} = 2.00$; alternative view.

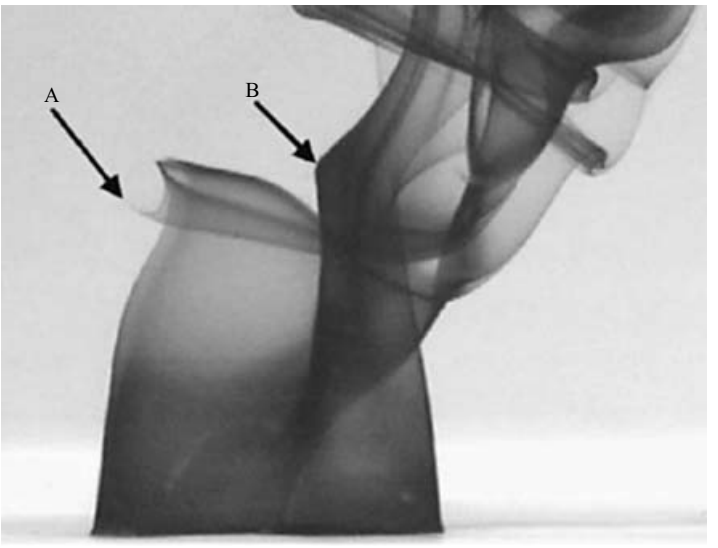

FIGURE 12. Water-tunnel dye visualization of a transverse jet at $r = 4.6$, $Re_j = 1600$, showing windward-side (A) and lee-side (B) roll-ups of the shear layer. Reproduced from Lim *et al.* (2001) with permission from the American Institute of Physics.

first few shear layer roll-ups), shear layer segments roll up either on their windward or lee sides but never on both; thus, true vortex rings are never formed. Instead, our simulations demonstrate that the lee and windward vortex loops evolve from successive, but similarly folding, segments of the jet shear layer.

Assembling additional segments of the shear layer offers further insight into the structure of the jet's near field. Figure 11 again shows the two shear layer segments described in the preceding paragraphs, but adds two subsequent shear layer segments to the picture. The green and blue elements represent vorticity introduced into the flow for $\tilde{t} \in [1.23, 1.26]$ and $\tilde{t} \in [1.28, 1.35]$ respectively. The green segment (i.e. group 3), shown unfolded in figure 11(*a*) and folded in figure 11(*b*), begins the transition to the next group of roll-ups. Like the preceding segments, it folds into two vortex arcs, but its vertical extent is much smaller. Its lee-side vorticity is not attracted to the vortex arc at the top of the figure; rather, it initiates a new lee-side vortex arc between the windward and lee arcs of segments 1 and 2. This new lee-side arc is marked 'c' in figure 11(*c*), while the older windward-side and lee-side arcs of segments 1 and 2 are marked 'b' and 'a,' respectively. Figure 11(*c*) also adds the fourth shear layer segment in its folded state. This segment rolls up strongly on its lee side, strengthening vortex arc 'c'; its windward side, though not rolled up strongly, points out the site of a new windward roll-up at the bottom of the figure, marked 'd'. In keeping with the overall alternating pattern, the next segment of the shear layer will reinforce the new windward roll-up. Successive pairs of shear layer segments thus create an interlocking structure of vortex arcs as they fold, i.e. vortex arcs 'a' and 'b' are interleaved by newer arcs 'c' and 'd'. An alternative perspective of all four shear layer segments at $\tilde{t} = 2.00$ is given in figure 11(*d*), showing the winding of vortex filaments around the arms of counter-rotating vorticity.

The periodic shear layer deformation mechanism just described is not unique to the $r = 7$ jet. We observe the same transformations of the shear layer at $r = 5$ and $r = 10$, and the same resulting pattern of lee and windward vortex arcs (Marzouk 2004).

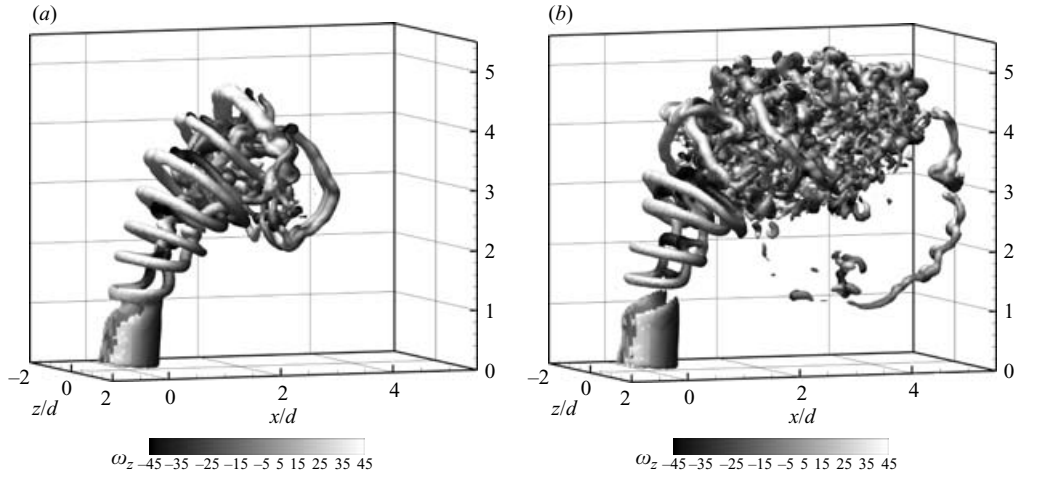

FIGURE 13. Vorticity magnitude isosurface $\|\boldsymbol{\omega}\|_2 = 45.0$ in the $r = 7$ jet, shown as contours of spanwise vorticity ω_z at two successive times: (*a*) $\tilde{t} = 1.80$, (*b*) $\tilde{t} = 2.40$.

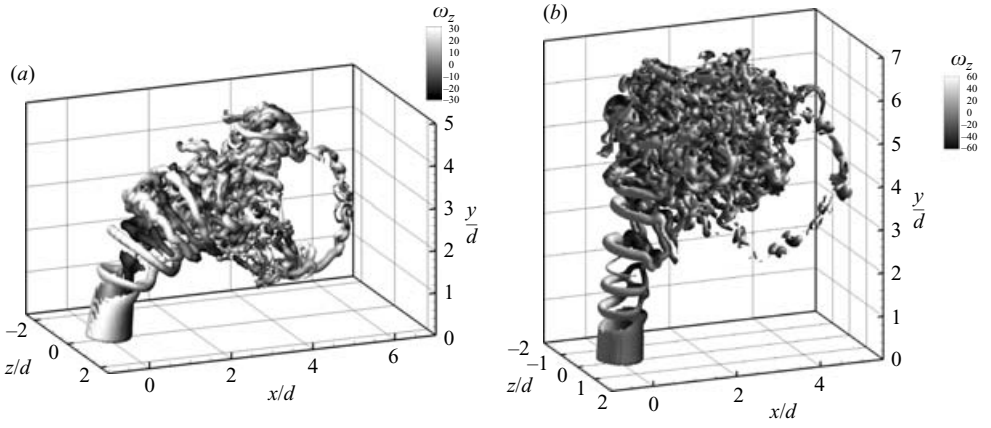

FIGURE 14. Vorticity magnitude isosurfaces, shown as contours of spanwise vorticity ω_z. (*a*) $r = 5$, $\tilde{t} = 3.00$; $\|\boldsymbol{\omega}\|_2 = 28.0$. (*b*) $r = 10$, $\tilde{t} = 1.80$; $\|\boldsymbol{\omega}\|_2 = 60.0$.

5.2.3. *Vorticity isosurfaces*

We turn our attention from transformations of the jet shear layer to direct examination of the vorticity field. The vorticity $\boldsymbol{\omega}(\boldsymbol{x}, t)$ is computed on nodes of a regular grid by summation over all the vortex elements, as specifed by (3.12). Grid spacing is $h = 0.05$; this three-dimensional mesh is then used to create vorticity isosurfaces and contours.

Figure 13 shows isosurfaces of vorticity magnitude $\|\boldsymbol{\omega}\|_2 = 45.0$ for the $r = 7$ jet at two successive times, $\tilde{t} = 1.8$ and 2.4. Analogous isosurfaces are computed for the two other jets. Figure 14 shows $\|\boldsymbol{\omega}\|_2 = 28.0$ isosurfaces for the $r = 5$ jet at $\tilde{t} = 3.0$ and $\|\omega\|_2 = 60.0$ isosurfaces for the $r = 10$ jet at $\tilde{t} = 1.8$.

Examination of these isosurfaces confirms the presence of several key vortical structures. Roll-up of the shear layer into vortex arcs is clearly visible at all values of r. Also apparent are arms of vorticity aligned with the jet trajectory on the lee side of

the jet; these arms seem connected to vortex arcs on the windward side, particularly among the first few roll-ups. This vorticity structure is consistent with the material deformations described in the previous section. The configuration of the vorticity arms – pulled upwards into the centre of the vortex arcs immediately above them – strengthens our hypothesis that vortical structures already in the flow induce the initial axial stretching of the jet shear layer on its lee side.

The relatively organized and periodic vortical structures in the intermediate field of the jet undergo a sudden breakdown into smaller length scales, 4–5 diameters from the nozzle for $r = 10$, 3–4 diameters from the jet nozzle for $r = 7$, and slightly closer for $r = 5$. In the vortex filament plots, this breakdown was manifested by a complex tangle of computational elements; here we observe a dense field of small fragmented isosurfaces. This transition is accompanied by more pronounced bending into the crossflow. Some larger-scale structures, e.g. interacting vortex arcs along the top edge of jet, are still visible, but the field is dominated by small length scales. Further downstream (e.g. for $x/d > 4.0$ at $r = 7$) there are artifacts of jet startup, such as a tongue of vortex-carrying fluid collapsing onto the centreplane. But the present simulations have continued long enough to show that the breakdown into small scales is a persistent feature of the flow.

Mechanisms discussed in § 5.2.2 suggest that vortex arcs carrying opposite-sign azimuthal vorticity are driven towards the windward boundary of the jet. This mechanism is also evident in figures 13 and 14. In each of these figures, the vorticity magnitude isosurfaces discussed above have also been contoured by the local spanwise vorticity ω_z. Negative spanwise vorticity, indicated by darker shading, originates on the lee side of the jet. As the jet penetrates, lee-side vortex arcs produced by roll-up and deformation of the shear layer find their way to the windward side. The resulting pattern is of vortex arcs carrying alternating signs of azimuthal vorticity, curved along the windward boundary of the jet.

A more detailed view of this pattern, and indeed of each transition in the vorticity structure of the jet, is given in figure 15 for the $r = 7$ jet at $\tilde{t} = 2.10$. Figure 15(*a*) shows the region immediately above the nozzle, where vorticity is largely confined to a cylindrical sheet. The vorticity magnitude isosurface is contoured by the wall-normal vorticity ω_y, and at the top of the figure, the first transition away from the cylindrical sheet configuration is visible: two arms of counter-rotating vorticity, aligned with the jet trajectory. These arms correspond to the 'tongue-like' structure identified in § 5.2.2 and depicted, for example, in figure 8(*c*). This tongue-like structure continues into the bottom of figure 15(*b*), where the top of the tongue has become the first lee-side vortex arc. In figure 15(*b*), the vorticity magnitude isosurface is contoured by ω_z, and thus the folding of material rings and the migration of lee-side vortex arcs with $\omega_z < 0$ toward the windward boundary are very much in evidence. Connected arms of counter-rotating vorticity persist on the lee side of the jet, approximately one diameter to either side of the centreplane. The winding of high-vorticity regions around these arms is particularly visible in figure 15(*c*). Figure 15(*d*) shows the final transition in vorticity structure, namely a breakup of the organized structures in figures 15(*b*) and 15(*c*) into smaller scales.

While merging of opposite-sign vortex arcs has been proposed by Eroglu & Breidenthal (2001) and was observed in our earlier, more dissipative, simulations (Marzouk & Ghoniem 2002), we do not explicitly observe merging here. Opposite-sign vortex arcs certainly approach each other more closely as the jet evolves, for instance at the top of figure 15(*b*, *c*) and at the bottom of figure 15(*d*). It is possible that the subsequent breakup into small scales may obscure any large-scale merging.

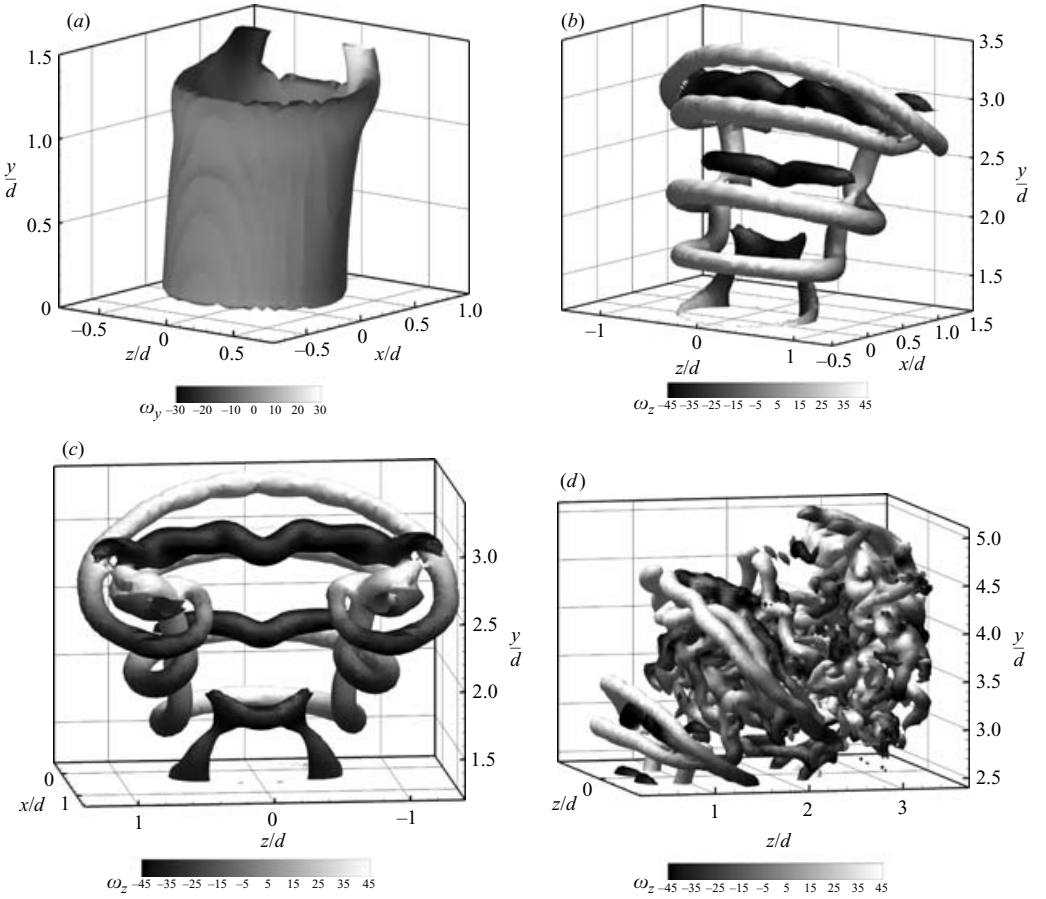

FIGURE 15. Vorticity magnitude isosurfaces at $\tilde{t} = 2.10$ in the $r = 7$ jet: (*a*) $\|\boldsymbol{\omega}\|_2 = 39.0$ contour ω_y; (*b*) $\|\boldsymbol{\omega}\|_2 = 45.0$ contoured by ω_z; (*c*) $\|\boldsymbol{\omega}\|_2 = 45.0$ contoured by ω_z, alternate view; (*d*) $\|\boldsymbol{\omega}\|_2 = 52.0$ contoured by ω_z. The plots show successive transitions from a cylindrical vortex sheet (*a*) to vortex arcs and arms of counter-rotating vorticity (*b*)–(*c*) to a breakdown into smaller scales (*d*).

It is also reasonable to expect that the mechanism and location of any merging may depend on Reynolds number; this dependence is under investigation.

A crucial feature of counter-rotating vorticity in the near field is that, though it results from periodic processes (e.g. roll-up and deformation of the shear layer), it persists in the mean field (Cortelezzi & Karagozian 2001; Rivero *et al.* 2001; Yuan *et al.* 1999). We investigate this feature by computing the time-average of the vorticity field over one cycle of shear layer roll-up. Shear layer roll-up in the near field is strongly periodic, with a period $\tilde{t}$ of approximately 0.18 in the $r = 7$ jet. This corresponds to a jet Strouhal number $St \equiv fd/U_j = fd/rU_\infty$ of 0.8, a value confirmed by examination of velocity fluctuations at selected points around the shear layer. Similarly, for the $r = 5$ jet we find a roll-up frequency of $St = 0.6$ and for the $r = 10$ jet, $St = 0.64$. Experimental measurements of the dominant St in the shear layer have varied widely, on the other hand. Karagozian *et al.* (2005) report a dominant St of 0.8 for $r = 7$ and $r = 8$ (matching our $r = 7$ result exactly), but a jump to higher frequencies ($St \approx 1.0$–1.1) for $r = 5$ and lower. Recent work by Karagozian *et al.* suggests that in addition to

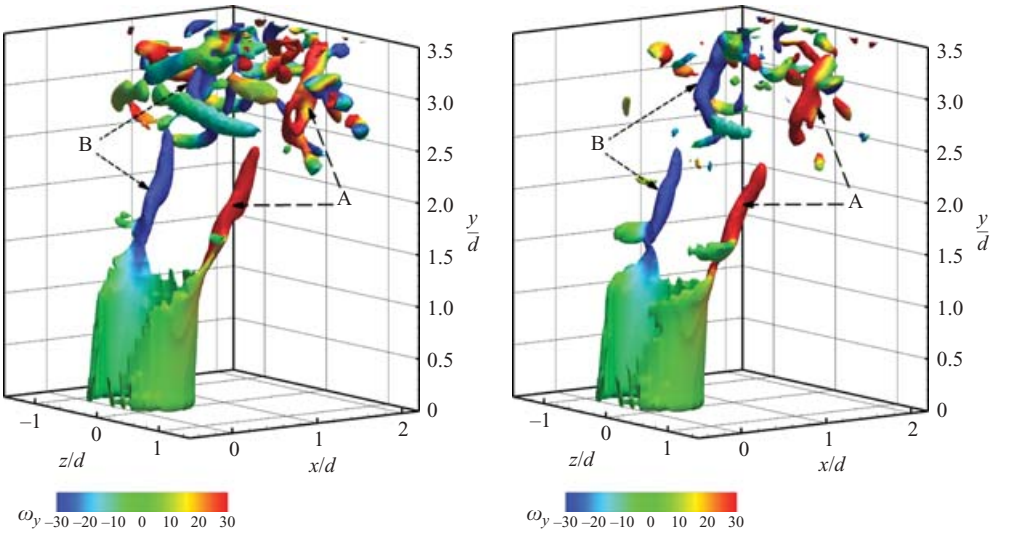

FIGURE 16. Isosurfaces $\|\bar{\boldsymbol{\omega}}\|_2 = 45.0$ contoured by mean wall-normal vorticity $\bar{\omega}_y$ in the $r = 7$ jet. (*a*) Mean vorticity field over the interval $\tilde{t} \in [2.31, 2.49]$, which corresponds to a single cycle of shear-layer roll-up. (*b*) Mean vorticity field over the interval $\tilde{t} \in [2.23, 2.49]$.

the velocity ratio, a host of other factors, e.g. jet Reynolds number, jet velocity profile, and jet-pipe boundary layer thickness, might influence these near-field frequencies.

We compute the averaged vorticity field in an $r = 7$ jet using realizations incrementally separated by $\Delta t = 0.02$ spanning a single shear layer roll-up period. Figure 16(*a*) shows the isosurface of vorticity magnitude $\|\bar{\boldsymbol{\omega}}\| = 45$ where $\bar{\boldsymbol{\omega}}$ is the mean vorticity in the interval $\tilde{t} \in [2.31, 2.49]$. The isosurface is contoured by the mean vertical vorticity $\bar{\omega}_y$. Two arms of counter-rotating vorticity, labelled 'A' and 'B', are present for $1 < y/d < 3.5$, while the remaining structures – the periodic vortex arcs of alternating sign on the windward side of the jet – have disappeared. Widening the interval over which averaging is performed to $\tilde{t} \in [2.23, 2.49]$ more clearly reveals a continued CVP section further along the trajectory, in figure 16(*b*). Since the length of this interval is not a multiple of near-field roll-up period, the near-field CVP is more cleanly isolated in figure 16(*a*). Both of these figures, however, show that the CVP is in fact the dominant feature of the mean vorticity field upstream of the breakup into smaller scales. Also, note that very little wall-normal vorticity is present in the first diameter of the trajectory. This observation is consistent with the mechanisms described in § 5.2.2, in which axial deformation of the shear layer gradually re-orients initially azimuthal vorticity to the wall-normal direction.

We now summarize observations from this section and §§ 5.2.1–5.2.2 to assemble a complete description of the near-field evolution of the jet shear layer:

(i) Vorticity in the nascent jet shear layer is oriented primarily, but not entirely, in the azimuthal direction. Wall-normal and azimuthal perturbations to the vorticity of the jet pipe boundary layer, resulting from interaction of the jet with the crossflow boundary layer, are essential to predicting the jet's initial upright trajectory (see §§ 4.2 and 5.4).

(ii) Deformations of the shear layer are induced in part by vorticity already in the flow. The evolution of vortical structures in the near field thus experiences an initial transient before settling to a periodic process. Shear layer segments in the mature near field evolve differently to those introduced immediately after jet startup.

(iii) In the mature near field, initially planar material rings on the shear layer undergo the following sequence of deformations: First, vorticity above and downstream of the orifice induces an upward stretching of the nascent shear layer on its lee side. On each ring, this deformation initiates arms of counter-rotating vorticity aligned with the jet trajectory. Counter-rotating vorticity in turn induces a velocity on material elements between these arms, pushing material elements which initially coincided with the lee edge of each ring towards the windward edge of the jet. Material rings thus fold completely, not into two segments normal to each other, as proposed by Kelso *et al.* (1996) and Cortelezzi & Karagozian (2001).

(iv) Every segment of shear layer undergoes the deformations described above. Superimposed on this process, however, is a series of roll-ups on the windward and lee sides of the jet. Successive segments of the shear layer alternately roll up more strongly on one side or the other. Lee-side roll-ups are initiated after upward deformation of the shear layer on its downstream edge, and thus are pushed towards the windward edge of the jet as each shear layer segment folds. Both groups of roll-ups correspond to vortex arcs visible as vorticity isosurfaces. However, because of their origins on opposite sides of the jet, they carry opposite signs of vorticity, even as they approach each other on the windward edge of the jet.

(v) Several diameters above the orifice, once the folding of material rings is complete, the near field of the jet has developed a complex interlocking vorticity structure, depicted in figures 10 and 11. While pairs of adjacent shear layer segments yield opposite-sign vortex arcs on the windward boundary, the vortex arcs generated by one pair of shear layer segments are interleaved by the vortex arcs of the subsequent pair.

(vi) The dynamics of the mature near field are essentially periodic, driven by the periodicity of shear layer roll-up. However, counter-rotating vorticity persists in and is indeed the dominant feature of the mean field. It is not clear whether opposite-signed vortex arcs on the windward boundary merge further downstream as near-field vortical structures break into small scales. The peak Strouhal number in the near field does not persist downstream, however.

(vii) In conjunction with these transformations of shear layer vorticity, we do not observe vortex breakdown in the near field as proposed by Yuan *et al.* (1999) and Kelso *et al.* (1996). These studies cite evidence of vortex breakdown less than a single diameter above the jet exit, though for flows with finite Reynolds numbers ($Re_{cf} \approx$ 1000–2000), appreciable upstream boundary layer thicknesses ($\delta/d \approx 0.50$–0.61), and somewhat smaller velocity ratios than those tested here ($r \approx 2$–6). In Yuan *et al.* vortex breakdown is manifested by a spread of vortex lines from the terminus of 'hanging vortices' formed on the lateral edges of the jet, and by a sudden decrease in axial velocity through these structures. Kelso *et al.* cite a region of reversed flow following the initiation of the CVP on either side of the centreplane. Though we observe vortical structures that are generally analogous to Kelso *et al.*, we do not reproduce these signs of vortex breakdown, nor are they apparent in other studies of the jet near field (Cortelezzi & Karagozian 2001). Vortex breakdown is quite sensitive to inlet conditions, e.g. the profile of the incoming jet flow, and differences in the flow parameters may also play a role; this phenomenon merits further investigation.

5.2.4. *Far-field vorticity structure and the transition to small scales*

The dramatic breakdown of organized vortical structures into smaller scales as the transverse jet bends into the crossflow has been observed elsewhere (Yuan *et al.* 1999), but mechanisms underlying this breakdown are not immediately clear. Classical

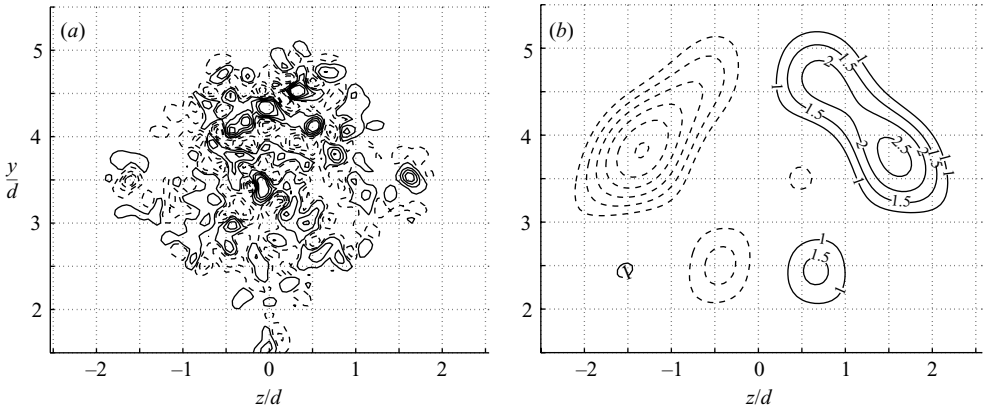

FIGURE 17. Instantaneous streamwise vorticity at $x/d = 2.25$, $\tilde{t} = 2.40$ in the $r = 7$ jet, before and after low-pass filtering. Solid contours indicate positive values; dashed contours indicate the corresponding negative values. (*a*) Instantaneous vorticity. Contour levels are $\omega_x = 5, 25, 45, 65$. (*b*) Filtered vorticity. Contour levels as marked.

instabilities of anti-parallel vortex tubes may be excited as counter-rotating vortex arcs approach each other on the windward boundary of the jet (Williamson, Leweke & Miller 2000), in particular, short-wave instabilities, excited when the distance between counter-rotating filaments is comparable to or smaller than a core size (Wang 1998; Chorin 1994). Whatever role these instabilities may play, one would like a more specific explanation of why the ladder-like structure of the intermediate field, exemplified by figure 15(*b*, *c*), consistently breaks down after 2–3 diameters of vertical extent, over a range of r. The winding of vortex arcs around CVP arms suggests that counter-rotating vorticity provides energy for sustained stretching of the anti-parallel vortex arcs confined to the windward boundary. Indeed, the stretching of material approaching the windward edge of the jet is consistent with ring deformations discussed in § 5.2.2. Stretching intensifies these anti-parallel vortical structures – the 'rungs' of the 'ladder' – and thus may precipitate their breakdown to space-filling small scales (exemplified in figure 15*d*). Our discussion here is merely conjectural, however, and the mechanisms underlying the transition to small scales merit further investigation.

Nonetheless, we can still make basic inquiries about vorticity structure in the far field. The complexity of this region observed in vorticity isosurface plots (e.g. figures 13 and 14) is also visible on instantaneous slices of streamwise vorticity. Our interest in streamwise vorticity is motivated by the traditional picture of the transverse jet far field, in which a counter-rotating vortex pair with compact cores slowly travels away from the wall and spreads as it persists downstream (Broadwell & Breidenthal 1984; Karagozian 1986). This picture, based on integral arguments or ensemble-averaged measurements of scalar concentration, vorticity, or velocity, is admittedly over-simplified. The instantaneous structure of the jet cross-section is far more complex: asymmetric, meandering in the spanwise and wall-normal directions, and dominated by small scales (Smith & Mungal 1998; Eiff & Keffer 1997; Rivero *et al.* 2001; Narayanan, Barooah & Cohen 2003). Figure 17(*a*) bears this out, showing streamwise vorticity on a plane of constant x/d in the breakdown region, for $r = 7$. The field is composed entirely of small-scale structures, with significant co-mingling of positive and negative vorticity. Streamwise vorticity on additional x/d-planes and at other values of r appears similar (Marzouk 2004).

Though the vorticity field appears quite unorganized, it may have an underlying structure; we would like to extract a signature of this structure if it is present. Following the approach suggested by Yuan *et al.* (1999), we low-pass filter the instantaneous streamwise vorticity in figure 17. We construct a two-dimensional low-pass filter with corner wavenumber $k_y = k_z = \pi/d$, where d is the jet diameter. Results of the filtering are shown in figure 17(*b*). Organized counter-rotation is evident in the filtered vorticity field, with strong regions of positive ω_x for $z > 0$ and vice versa, as expected. The maximum streamwise vorticity magnitude in the filtered field is approximately 8 times lower than in the unfiltered field; again, this result is consistent with Yuan *et al.* (1999). Weakening of the large-scale counter-rotation in the far field is also consistent with an energy transfer in the intermediate field from coherent CVP arms to small scales that originate in lee-side vortex arcs.

The instantaneous vorticity in figure 17 is slightly asymmetric about the centreplane ($z = 0$). Asymmetry persists under filtering, and we find that it is slightly more pronounced in the $r = 7$ case than in the $r = 5$ case (Marzouk 2004). Interpretation of this asymmetry and its origins is rather subtle. Though our vorticity-flux boundary conditions are symmetric and the crossflow is uniform, symmetry is not explicitly enforced elsewhere in the computation. In fact the clustering partition, with its random seed of initial centroids (see Marzouk & Ghoniem 2005) does not respect symmetry at all. As a result, 'noise' in the form of velocity approximation errors is distributed asymmetrically in space. These errors, in turn, may perturb vortex particle locations and weights asymmetrically.

Numerical observations, however, cannot be separated from the underlying flow physics. In a simulation, various forms of numerical error (e.g. approximation errors and roundoff error from finite-precision arithmetic) are always present; similarly, no experimental set-up can be free of physical noise, surface roughness, or asymmetry at length scales smaller than measurement or machining accuracy. Issues of symmetry are intimately linked to how the flow amplifies or dampens these perturbations. In general, questions of whether the transverse jet is ultimately 'symmetric' or 'asymmetric' remain unresolved. Smith & Mungal (1998) performed a series of wind tunnel experiments in which symmetry of the experimental set-up and flow uniformity were carefully controlled, yet they report instantaneous and even ensemble-averaged PLIF images of the jet cross-section that are not symmetric. Spatially filtered streamwise vorticity contours reported in Yuan *et al.* (1999) are also asymmetric, though in this computational study, the incoming pipe velocity profiles were extracted from a temporally evolving 'turbulent flow' simulation which may have had instantaneous asymmetry. Several researchers have observed asymmetry in averaged profiles of the transverse jet, increasing with r and with downstream distance (Kamotani & Greber 1972; Smith & Mungal 1998).

Analysis of the filtered vorticity field raises another interesting issue: the impact of Reynolds number. Our earliest vortex simulations of this flow employed core expansion and consequently were quite dissipative in the far field; despite the coarseness of those calculations, counter-rotating streamwise vorticity was immediately evident in instantaneous transverse planes (Marzouk & Ghoniem 2002). Some of our ongoing work focuses on finite-Reynolds-number simulations of the transverse jet using vorticity redistribution (Wee, Marzouk & Ghoniem 2005); there the breakdown of organized structures into small scales remains very much in evidence, but it may be that the filtered vorticity field carries a proportionally larger portion of the energy. The large-eddy simulation study by Yuan *et al.* (1999) at a crossflow Reynolds number ($Re_{cf} = U_\infty d/\nu$) of 1050 shows results similar to the present data.

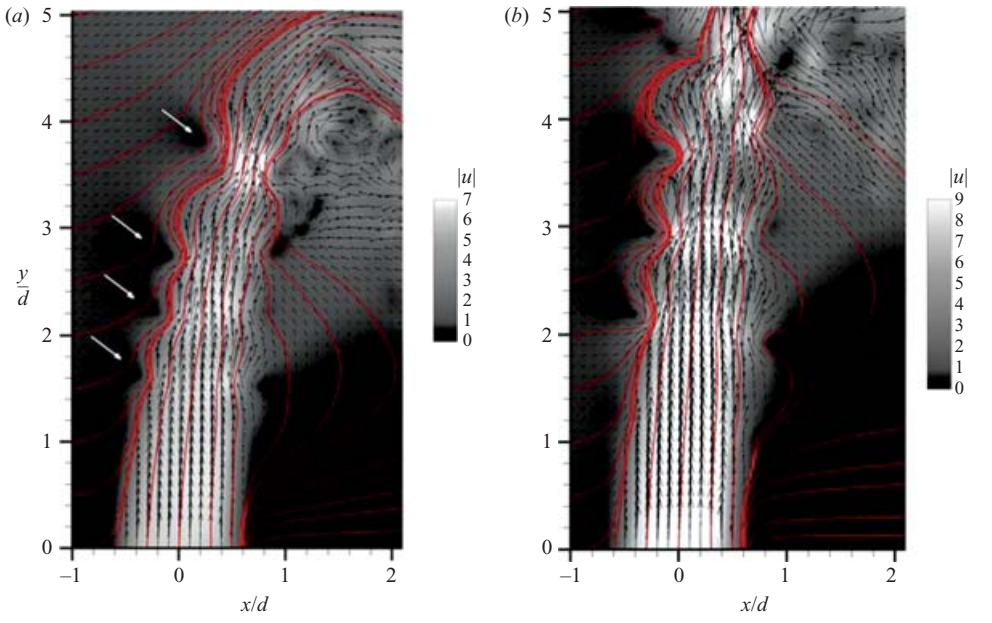

FIGURE 18. Instantaneous velocity field and streamlines in the centreplane $z = 0$: (*a*) $r = 7$, $\tilde{t} = 2.24$, (*b*) $r = 10$, $\tilde{t} = 1.68$. Contours indicate total velocity magnitude.

Water-tunnel experiments for extremely low Reynolds number ($Re = 21$–78), however, show that the jet fluid can completely bifurcate into tubes aligned with counter-rotating vorticity (Huq & Dhanak 1996).

5.3. *Velocity field and jet trajectory*

Figure 18 shows instantaneous velocity vectors and streamlines on the centreplane ($z = 0$) for transverse jets at $r = 7$ and 10. Contour shading indicates the total velocity magnitude $\|\boldsymbol{u}\|_2$. Though we focus primarily on the $r = 7$ case, features noted below are common to all of the velocity ratios considered in this work.

First, the initial orientation of each jet is upright, nearly normal to the wall. As detailed in § 4.2, the azimuthal variation of each vorticity component along the nascent jet–crossflow interface has a significant impact on the near-field trajectory. Low-velocity regions along the windward edge of each jet correspond to the cores of vortex arcs resulting from shear-layer roll-up. Arrows in figure 18(*a*) highlight these cores for the $r = 7$ jet. Vortex cores seem regularly spaced for the first few diameters following the initial roll-up, reflecting the periodicity of this process in the near field, but this regularity disappears further downstream. PLIF images of the centreplane obtained by Rivero *et al.* (2001) show a similar disruption of regular windward-side roll-ups as the jet bends downstream.

Convergent streamlines immediately downstream of the jet nozzle suggest a node at or near the wall. Hasselbrink & Mungal (2001*b*) confirm the presence of such a node in PIV measurements at $r = 10$, though for an elevated jet. Hot-wire measurements by Kelso *et al.* (1996) find a similar node very near the wall at lower r. This two-dimensional 'source' node corresponds to fluid being swept toward the centreplane on the lee side of the jet. By continuity, the lee side of the jet shear layer is initially subject to a compressive strain rate ($\partial w/\partial z < 0$) as it is pulled upwards.

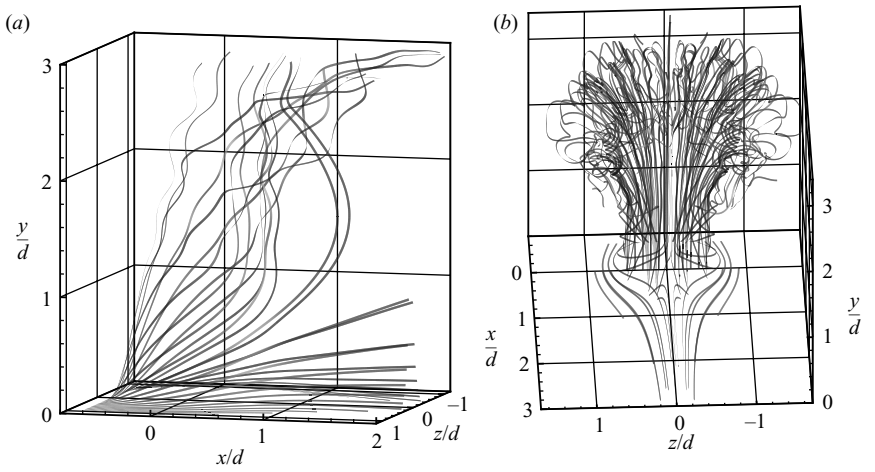

FIGURE 19. Three-dimensional instantaneous velocity streamlines in the $r = 7$ jet at $\tilde{t} = 2.00$. (*a*) Streamlines originating in the crossflow, upstream of the orifice; side view. (*b*) Streamlines placed throughout the flow; downstream view.

Three-dimensional streamlines, shown at $\tilde{t} = 2.00$ in figure 19, provide a more complete context for features on the centreplane. Figure 19(*a*) shows only streamlines originating in the crossflow. Upstream of the orifice, near the centreplane, streamlines are immediately pulled upwards into the windward face of the jet. Thus, flow divergence from the centreplane on the windward side of the jet is generally weak, i.e. there is no 'sink' node upstream of the orifice analogous to the 'source' node on the opposite side. As Hasselbrink & Mungal (2001*b*) remark, this is yet another indication of how the transverse jet flow field fundamentally differs from flow around a cylinder.

Further away from the centreplane, streamlines are simultaneously swept upwards and around the jet column. Streamlines passing closer to the edges of the orifice are pulled up more strongly than those further outside. Streamlines originating sufficiently far upstream or sufficiently far from the centreplane lead primarily around the nascent jet column and into the centreplane on the lee side of the jet, consistent with our boundary conditions.

On the lee side of the jet, some of the crossflow fluid is pulled strongly upwards into the region of counter-rotating vorticity, while other streamlines continue in the streamwise direction near the wall. Hot-wire measurements by Kelso *et al.* (1996) reveal similar flow patterns both on the centreplane and around the jet orifice, corroborated by Schlüter & Schönfeld (2000) in a computational study. Upward-pointing streamlines on the lee side of the jet are consistent with entrainment mechanisms in the far field reported by Yuan & Street (1998). In fact, scalar transport simulations by Yuan & Street reveal a region of crossflow fluid at the centreplane, between CVP structures, on the lee side of the jet.

Figure 20 compares the computed transverse jet trajectories with several experimental data sets, using rd-scaled coordinates (Pratte & Baines 1967; Broadwell & Breidenthal 1984; Hasselbrink & Mungal 2001*a*). Trajectories from the our simulations are defined by the streamline emanating from the centre of the jet orifice, with the velocity field averaged over a single-shear layer roll-up period. Note that Smith & Mungal (1998) ('SM' in the figure legend) define the trajectory as the locus of

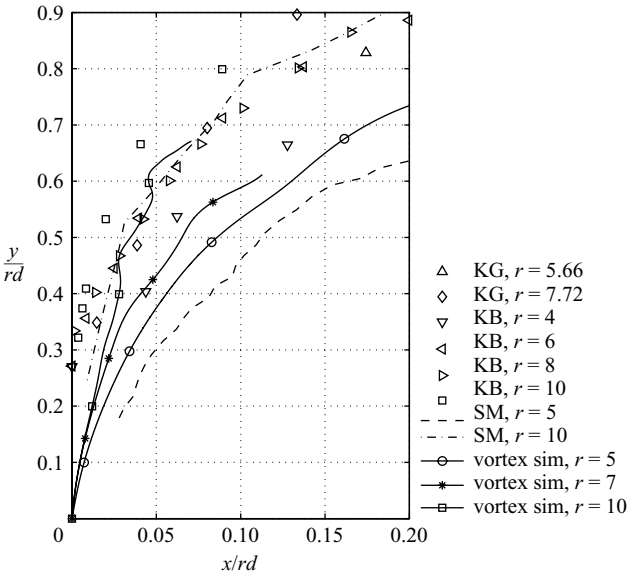

FIGURE 20. Center streamline trajectories in rd-coordinates compared with experimental data. KB = Keffer & Baines (1962); KG = Kamotani & Greber (1972, 1974); SM = Smith & Mungal (1998).

maximum scalar concentration on the centreplane, while Kamotani & Greber (1972, 1974) ('KG' in the figure legend) use the locus of maximum velocity. These definitions, along with differences in Reynolds number (Yuan & Street 1998) and in the velocity profiles of the jet and crossflow (Muppidi & Mahesh 2005) may account for much of the observed scatter among the experimental measurements. Nonetheless, the computed trajectories display reasonable agreement with the experimental data, certainly falling within the scatter. We only present computational data that have reached a stationary state, i.e. where no substantial further changes in the jet envelope are observed.

5.4. *Near-field vorticity structure*

The discussion of vorticity-flux boundary conditions in § 4.2 can be extended to provide an analytical description of vortex lines in the near field of the transverse jet, just above the orifice. The geometry of these vortex lines is particularly interesting in the context of the folding mechanisms responsible for the vortical structure of the near field, and in the light of several previous studies of near-field vorticity (Sykes *et al.* 1986; Coelho & Hunt 1989). An analytical description of nascent vortex lines could also be used to reformulate the present simulations in terms of closed vortex filaments, rather than vortex sticks, though we do not pursue such a development here.

Following the derivation detailed in § 4.2, we can write the vorticity field near the nozzle, i.e. for $0 < y/d \ll 1$, as:

$$\begin{aligned}\boldsymbol{\omega}_i \,\mathrm{d}V_i &= \left(-\frac{r^2}{4} - \frac{r}{4}\cos\theta_i\right)\Delta t_{noz}\Delta\theta\hat{\boldsymbol{e}}_\theta + \left(\frac{r}{4}\sin\theta_i - y\frac{r}{2}\sin\theta_i\right)\Delta t_{noz}\Delta\theta\hat{\boldsymbol{e}}_y \\ &= \Gamma_i \,\mathrm{d}\boldsymbol{l}_i(\theta, y). \end{aligned} \tag{5.1}$$

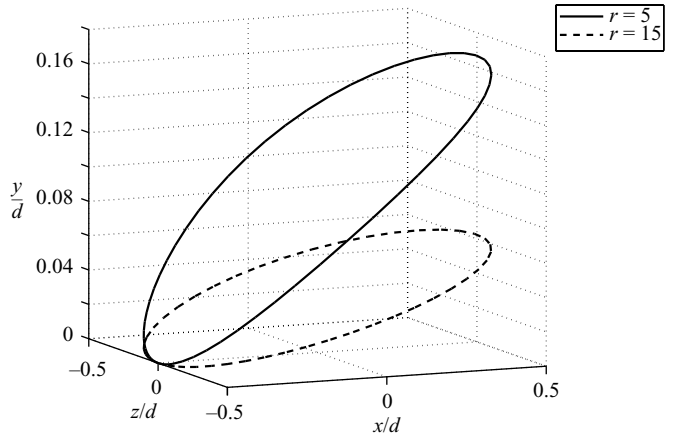

FIGURE 21. Geometry of vortex lines above the orifice of the transverse jet for different r, according to the analytical model in § 5.4.

Dividing by the desired filament circulation $\Gamma = \frac{1}{2}r^2\Delta t$, we seek integral curves of the vector field

$$\boldsymbol{l}(\theta, y) = -\left(1 + \frac{\cos\theta}{r}\right)\hat{\boldsymbol{e}}_\theta + \frac{\sin\theta}{r}(1-2y)\hat{\boldsymbol{e}}_y. \tag{5.2}$$

The resulting space curve $\boldsymbol{\zeta}(s) : (R, \theta, y) = (1/2, p(s), q(s))$ can be obtained as the solution of two ODEs:

$$\left.\begin{aligned} \frac{\mathrm{d}p}{\mathrm{d}s} &= -\left(1 + \frac{\cos p}{r}\right), \\ \frac{\mathrm{d}q}{\mathrm{d}s} &= \frac{\sin p}{2r}(1-2q). \end{aligned}\right\} \tag{5.3}$$

A solution of these coupled ODEs can be written analytically. Choosing initial conditions so that $(\theta, y) = (\pi, 0)$ is a point on $\boldsymbol{\zeta}(s)$, we have

$$p(s) = -2\arctan\left(\mathscr{I}\sqrt{\frac{r+1}{r-1}}\right) \tag{5.4}$$

$$q(s) = \frac{r}{(r-1)^2(r+1)^2}\left(r - \frac{1-\mathscr{I}^2}{1+\mathscr{I}^2}\right)^2 + \frac{\mathscr{I}^2(\mathscr{I}^2 r + r - 1)}{(r-1)^2(1+\mathscr{I}^2)^2} \tag{5.5}$$

where

$$\mathscr{I} \equiv \tan\left(\frac{s}{2}\sqrt{1 - \frac{1}{r^2}}\right) \tag{5.6}$$

and the solution is $(2\pi/\sqrt{1-1/r^2})$-periodic in the parameter s. For larger r, the resulting vortex filament is relatively flat and ring-like, as jet azimuthal vorticity dominates; for smaller r, the vortex filament has a greater vertical extent and is slightly 'kinked' in the y-direction. The geometry of vortex filaments above the jet orifice is illustrated in figure 21 for $r = 5$ and $r = 15$.

A confirmation of this analytical model is presented in figure 22. Here, the solid curves are vortex lines of the numerical vorticity field, i.e. lines obtained by numerical integration of the vorticity of an $r = 7$ jet at $\tilde{t} = 1.40$, a time by which the vorticity field several diameters above the jet nozzle has matured. Dashed lines are obtained from

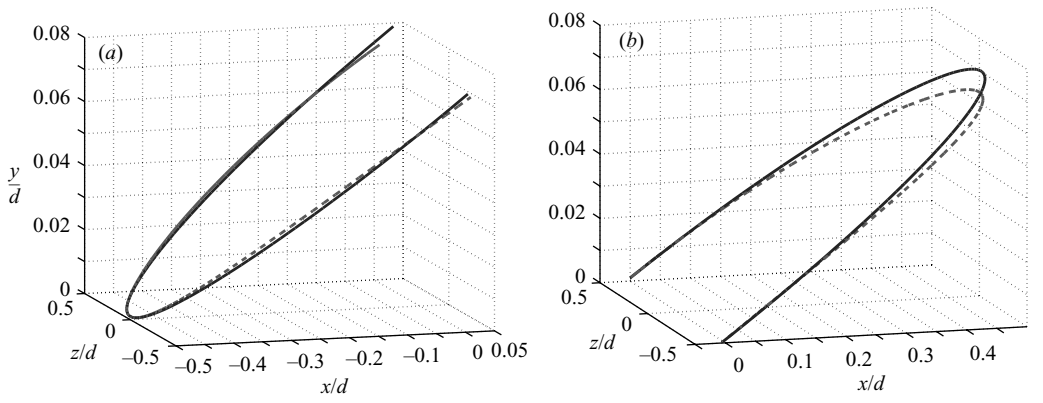

FIGURE 22. Comparison of analytical and numerical vortex lines in the near field of the transverse jet, $r = 7$: (*a*) back half of jet orifice, (*b*) pront half of jet orifice. Solid lines are integral curves of the numerical vorticity field at $\tilde{t} = 1.4$; dashed lines represent the analytical expression.

integration of the ODE system in (5.3). Agreement is quite good. Slight discrepancies may be due in part to the finite spatial resolution of the numerical vorticity field, here obtained for $\delta = 0.05$, $h/\delta < 1$, compared to the continuous field used to derive the analytical filaments.

Vortex lines in the near field were also obtained by Sykes *et al.* (1986), for r ranging from 2 to 8. Though extracted from a Reynolds-averaged simulation, vortex lines near the nozzle show strong qualitative agreement with our present model, tilting upwards on the lee side of the orifice. Furthermore, in accordance with figure 21, Sykes *et al.* note that the 'relative importance of the initial vertical component decreases with increasing r'.

The three-dimensional entraining vortex sheet model of Coelho & Hunt (1989) also focuses on the near field but does not specify components of vorticity on the sheet *a priori*; it is instead formulated as a boundary value problem in terms of velocity potentials inside and outside the sheet. However, solutions for this model agree with the present vorticity formulation in a number of important respects. Coelho & Hunt emphasize that interactions between axial and azimuthal components of vorticity lead to an enhancement of azimuthal vorticity on the lee side of the sheet, consistent with the first term of (5.1). Initially planar material rings released in the jet boundary are lifted upwards on their lee sides, mirroring the initial stage of the ring deformations discussed in § 5.2.2. Filament geometries derived in the present work (which are essentially a reformulation of the vorticity-flux boundary conditions in § 4.2) are in a sense 'initial conditions' for the strength of the three-dimensional vortex sheet.

6. Summary and conclusions

This work has sought a detailed, mechanistic understanding of vorticity dynamics in the transverse jet. We first consider vorticity generation mechanisms. A new formulation of vorticity-flux boundary conditions, developed in § 4, accounts for the interaction of channel-wall vorticity with the jet flow immediately around the nozzle edge. We demonstrate that the nascent jet shear layer must contain not only azimuthal vorticity generated in the jet pipe, but wall-normal and azimuthal components

resulting from the jet–crossflow interaction. These components are essential to predicting near-field jet trajectories consistent with experimental results. Our formulation also yields analytical expressions for vortex lines in the near field of the jet.

Vorticity generation mechanisms thus provide a foundation for the central question of this study: how vorticity entering the flow is transformed into coherent vortical structures. Our approach is computational. We develop a three-dimensional vortex simulation of the transverse jet at large Reynolds number and examine the evolution of the jet at three velocity ratios, $r = 5$, 7, and 10. In all three cases, simulations resolve transformations of the cylindrical shear layer emanating from the nozzle. Initially dominated by azimuthal vorticity, the lee side of the shear layer is stretched axially by existing vortical structures to form arms of counter-rotating vorticity aligned with the jet trajectory. Periodic roll-up of the shear layer accompanies this deformation, creating alternate vortex arcs on the lee and windward sides of the jet. Counter-rotating vorticity then drives lee-side roll-ups in the windward direction, along the normal to the jet trajectory. Azimuthal vortex arcs of alternating sign thus approach each other on the windward boundary of the jet. Accordingly, initially planar material rings on the shear layer fold completely and assume an interlocking structure that persists for several diameters above the jet exit.

Though the near field of the jet is dominated by deformation and periodic roll-up of the shear layer, the resulting counter-rotating vorticity is a pronounced feature of the mean field; in turn, the mean counter-rotation influences the deformation of the shear layer.

Insight into these deformations comes from analysis of vorticity isosurfaces (§ 5.2.3) and time-resolved tracking of vorticity-carrying material elements (§ 5.2.2). Isosurfaces directly visualize the vorticity structure of the flow, indicating where vorticity is concentrated and how it is oriented. Tracking material elements and seeking a correspondence between these elements and emergent vortical structures addresses the mechanistic questions: the relationship beween the various vortical structures and the processes by which they form.

A final transition in vorticity structure accompanies the bending of the trajectory into the crossflow, and consists of a sharp breakdown of organized periodic structures into a dense distribution of smaller scales. The mechanism underlying this breakdown is not clear, but spatial filtering of the region downstream of the breakdown reveals the background persistence of counter-rotating streamwise vorticity.

We briefly outline some avenues for future work. First, while inviscid dynamics play a dominant role in the transverse jet, questions remain regarding the effect of Reynolds number, some of which we have noted in § 5. In particular, to what extent does the instantaneous structure of the far-field CVP depend on Re? Is the far-field transition to small scales more gradual at lower Re? Do opposite-signed vortex arcs on the windward side of the jet merge at lower Re? Does Re affect the near-field roll-up pattern on the shear layer? We will address these questions with finite-Reynolds-number vortex particle simulations (Wee & Ghoniem 2006).

Finite-Reynolds-number vortex methods should also render longer-time simulations more computationally feasible. Extending the present simulations of the transverse jet to longer times will yield mean trajectories that are stationary over wider regions of the flow. Achieving a stationary state for $y/rd \gg 1$ would allow comparison with far-field trajectory correlations, and perhaps even enable investigation of the relationship between topological changes in the vorticity field and the transition between near- and far-field regions of intermediate-asymptotic similarity.

This research is supported by the US Department of Energy, Office of Science, MICS. Computational support is provided by the National Energy Research Supercomputing Center (NERSC). Y. M. Marzouk also acknowledges the support of a graduate fellowship from the Fannie and John Hertz Foundation. This research was further supported by an appointment to the Sandia National Laboratories Truman Fellowship, sponsored by Sandia Corporation (a wholly owned subsidiary of Lockheed Martin Corporation) as operator of Sandia National Laboratories under US Department of Energy contract number DE-AC04-94AL85000. The authors also thank J. W. M. Bush, G. Haller, and the anonymous referees for their useful remarks.

REFERENCES

Andreopoulos, J. & Rodi, W. 1984 Experimental investigation of jets in a cross-flow. *J. Fluid Mech.* **138**, 93–127.

Ashurst, W. T. & Meiburg, E. 1988 Three-dimensional shear layers via vortex dynamics. *J. Fluid Mech.* **189**, 87–116.

Batchelor, G. K. 1973 *An Introduction to Fluid Dynamics*. Cambridge University Press.

Beale, J. T. & Majda, A. 1985 High-order accurate vortex methods with explicit velocity kernels. *J. Comput. Phys.* **58**, 188–208.

de Boor, C. 1978 *A Practical Guide to Splines*. Springer.

Broadwell, J. E. & Breidenthal, R. E. 1984 Structure and mixing of a transverse jet in incompressible-flow. *J. Fluid Mech.* **148**, 405–412.

Chang, Y. K. & Vakili, A. D. 1995 Dynamics of vortex rings in cross-flow. *Phys. Fluids* **7** (7), 1583–1597.

Chorin, A. J. 1973 Numerical study of slightly viscous flow. *J. Fluid Mech.* **57**, 785–796.

Chorin, A. J. 1993 Hairpin removal in vortex interactions II. *J. Comput. Phys.* **107**, 1–9.

Chorin, A. J. 1994 *Vorticity and Turbulence*. Springer.

Chorin, A. J. 1996 Microstructure, renormalization, and more efficient vortex methods. *ESAIM Proceedings: Vortex Flows and Related Numerical Methods II* vol. 1, pp. 1–14.

Chorin, A. J. & Hald, O. H. 1995 Vortex renormalization in three space dimensions. *Phys. Rev.* B **51** (17), 11969–11972.

Chorin, A. J. & Marsden, J. E. 1993 *A Mathematical Introduction to Fluid Mechanics*. Springer.

Coelho, S. L. V. & Hunt, J. C. R. 1989 The dynamics of the near-field of strong jets in crossflows. *J. Fluid Mech.* **200**, 95–120.

Cortelezzi, L. & Karagozian, A. R. 2001 On the formation of the counter-rotating vortex pair in transverse jets. *J. Fluid Mech.* **446**, 347–373.

Cottet, G.-H. & Koumoutsakos, P. D. 2000 *Vortex Methods: Theory and Practice*. Cambridge University Press.

Eiff, O. S. & Keffer, J. F. 1997 On the structures in the near-wake region of an elevated turbulent jet in a crossflow. *J. Fluid Mech.* **333**, 161–195.

Eroglu, A. & Breidenthal, R. E. 2001 Structure, penetration, and mixing of pulsed jets in crossflow. *AIAA J.* **39** (3), 417–423.

Fearn, R. & Weston, R. P. 1974 Vorticity associated with a jet in a cross flow. *AIAA J.* **12** (12), 1666–1671.

Fric, T. F. & Roshko, A. 1994 Vortical structure in the wake of a transverse jet. *J. Fluid Mech.* **279**, 1–47.

Hasselbrink, E. F. & Mungal, M. G. 2001*a* Transverse jets and jet flames. Part 1. Scaling laws for strong transverse jets. *J. Fluid Mech.* **443**, 1–25.

Hasselbrink, E. F. & Mungal, M. G. 2001*b* Transverse jets and jet flames. Part 2. Velocity and OH field imaging. *J. Fluid Mech.* **443**, 27–68.

Haven, B. A. & Kurosaka, M. 1997 Kidney and anti-kidney vortices in crossflow jets. *J. Fluid Mech.* **352**, 27–64.

Huq, P. & Dhanak, M. R. 1996 The bifurcation of circular jets in crossflow. *Phys. Fluids* **8** (3), 754–763.

Kamotani, Y. & Greber, I. 1972 Experiments on a turbulent jet in a cross flow. *AIAA J.* **10**, 1425–1429.

Kamotani, Y. & Greber, I. 1974 Experiments on confined turbulent jets in cross flow. *Tech. Rep.* CR-2392. NASA.

Karagozian, A. R. 1986 An analytical model for the vorticity associated with a transverse jet. *AIAA J.* **24**, 429–436.

Karagozian, A. R., Megerian, S., Alves, L., George, M., Kelly, R. E. & M'Closkey, R. T. 2005 Control of vorticity generation in an acoustically excited jet in crossflow. *AIAA Paper* 2005-0303.

Keffer, J. F. & Baines, W. D. 1962 The round turbulent jet in a cross-wind. *J. Fluid Mech.* **15**, 481–496.

Kelso, R. M., Lim, T. T. & Perry, A. E. 1996 An experimental study of round jets in cross-flow. *J. Fluid Mech.* **306**, 111–144.

Kelso, R. M. & Smits, A. J. 1995 Horseshoe vortex systems resulting from the interaction between a laminar boundary-layer and a transverse jet. *Phys. Fluids* **7** (1), 153–158.

Knio, O. M. & Ghoniem, A. F. 1990 Numerical study of a three-dimensional vortex method. *J. Comput. Phys.* **86**, 75–106.

Krothapalli, A., Lourenco, L. & Buchlin, J. M. 1990 Separated flow upstream of a jet in a cross-flow. *AIAA J.* **28** (3), 414–420.

Leonard, A. 1985 Computing three-dimensional incompressible flows with vortex elements. *Annual Review of Fluid Mechanics* **17**, 523–559.

Lim, T. T., New, T. H. & Luo, S. C. 2001 On the development of large-scale structures of a jet normal to a cross flow. *Phys. Fluids* **13** (3), 770–775.

Lindsay, K. & Krasny, R. 2001 A particle method and adaptive treecode for vortex sheet motion in three-dimensional flow. *J. Comput. Phys.* **172** (2), 879–907.

Margason, R. J. 1993 Fifty years of jet in cross flow research. In *Computational and Experimental Assessment of Jets in Cross Flow*, vol. CP-534. AGARD.

Marzouk, Y. M. 2004 Vorticity structure and evolution in a transverse jet with new algorithms for scalable particle simulation. PhD thesis, Massachusetts Institute of Technology.

Marzouk, Y. M. & Ghoniem, A. F. 2002 Mechanism of streamwise vorticity formation in a transverse jet. *AIAA Paper* 2002-1063.

Marzouk, Y. M. & Ghoniem, A. F. 2005 K-means clustering for optimal partitioning and dynamic load balancing of parallel hierarchical N-body simulations. *J. Comput. Phys.* **207**, 493–528.

Muppidi, S. & Mahesh, K. 2005 Study of trajectories of jets in crossflow using direct numerical simulations. *J. Fluid Mech.* **530**, 81–100.

Narayanan, S., Barooah, P. & Cohen, J. M. 2003 Dynamics and control of an isolated jet in crossflow. *AIAA J.* **41** (12), 2316–2330.

Pratte, B. D. & Baines, W. D. 1967 Profiles of the round turbulent jet in a cross flow. *J. Hydraul. Div, ASCE* **92**, 53–64.

Rivero, A., Ferre, J. A. & Giralt, F. 2001 Organized motions in a jet in crossflow. *J. Fluid Mech.* **444**, 117–149.

Rosenhead, L. 1931 The formation of vortices from a surface of discontinuity. *Proc. R. Soc. Lond.* A **134**, 170–192.

Schlüter, J. U. & Schönfeld, T. 2000 LES of jets in cross flow and its application to a gas turbine burner. *Flow Turbulence Combust.* **65** (2), 177–203.

Smith, S. H. & Mungal, M. G. 1998 Mixing, structure, and scaling of the jet in crossflow. *J. Fluid Mech.* **357**, 83–122.

Sykes, R. I., Lewellen, W. S. & Parker, S. F. 1986 On the vorticity dynamics of a turbulent jet in a cross-flow. *J. Fluid Mech.* **168**, 393–413.

Wang, H. Y. 1998 Short wave instability on vortex filaments. *Phys. Rev. Lett.* **80** (21), 4665–4668.

Wee, D. & Ghoniem, A. F. 2006 Modified interpolation kernels for diffusion and remeshing in vortex methods. *J. Comput. Phys.* **213** (1), 239–263.

Wee, D., Marzouk, Y. M. & Ghoniem, A. F. 2005 Lagrangian simulation of a jet in crossflow at a finite Reynolds number. *AIAA Paper* 2005-0291.

Williamson, C. H. K., Leweke, T. & Miller, G. D. 2000 Fundamental instabilities in spatially-developing wing wakes and temporally-developing vortex pairs. In *Turbulence Structure and Vortex Dynamics* (ed. J. C. R. Hunt & J. C. Vassilicos), pp. 83–103. Cambridge University Press.

Winckelmans, G. S. & Leonard, A. 1993 Contributions to vortex particle methods for the computation of three-dimensional incompressible unsteady flows. *J. Comput. Phys.* **109** (2), 247–273.

Yuan, L. L. & Street, R. L. 1998 Trajectory and entrainment of a round jet in crossflow. *Phys. Fluids* **10** (9), 2323–2335.

Yuan, L. L., Street, R. L. & Ferziger, J. H. 1999 Large-eddy simulations of a round jet in crossflow. *J. Fluid Mech.* **379**, 71–104.

Zaman, K. B. M. Q. & Foss, J. K. 1997 The effect of vortex generators on a jet in a cross-flow. *Phys. Fluids* **9** (1), 106–114.